

1 Fat2 polarizes the WAVE complex *in trans* to align 2 cell protrusions for collective migration

3 Audrey M. Williams¹, Seth Donoughe¹, Edwin Munro^{1,2,3}, Sally Horne-Badovinac^{1,2,*}

5 **Abstract**

6 For a group of cells to migrate together, each cell must couple the polarity of its own migratory machinery with
7 that of the other cells in the migrating group. Although collective cell migrations are common in animal de-
8 velopment, it is not understood how protrusions are coherently polarized within groups of migrating epithelial
9 cells. We address this problem in the collective migration of the *Drosophila melanogaster* follicular epithelial
10 cells, demonstrating that the atypical cadherin Fat2 relays polarity information between neighboring cells, caus-
11 ing them to align their lamellipodia and migrate together. Fat2 localizes the WAVE complex to the leading edge
12 of each cell, where the WAVE complex builds polarized lamellipodia. In Fat2's absence, the WAVE complex be-
13 comes enriched at fluctuating positions around the cell perimeter, resulting in short-lived and spatially disordered
14 protrusive regions, ultimately causing collective migration to fail. In wild-type tissue, Fat2 puncta along the trail-
15 ing edge of each cell concentrate the WAVE complex in corresponding puncta just across the cell-cell interface,
16 restricting WAVE complex activity and protrusions to one stable leading edge. In summary, migrating cells cou-
17 ple their protrusive activity to that of their neighbors using a polarized transmembrane cue. We propose that this
18 mechanism enables the tissue to achieve persistent, days-long directed migration.

19 **Introduction**

20 Collective cell migration is essential for a variety of morphogenetic processes in animals¹⁻⁴. As with individual
21 cell migrations, adherent collective migrations are driven by the concerted action of cell protrusions, contractile
22 actomyosin networks, and adhesions to a substrate^{2,5,6}. To move forward, individual cells polarize these structures
23 along a migratory axis, and to move persistently in one direction, they need to maintain that polarity stably over
24 time⁷. Collective cell migrations introduce a new challenge: to move together, the group of migrating cells must
25 be polarized in the same direction⁷. Otherwise, they would exert forces in different directions and move less
26 efficiently, separate, or fail to migrate altogether.

27 The epithelial follicle cells of the *Drosophila melanogaster* ovary are a powerful experimental system in which to
28 investigate how local interactions among migrating cells establish and maintain group polarity. Follicle cells are

*Corresponding author. E-mail: shorne@uchicago.edu

¹Department of Molecular Genetics and Cell Biology, University of Chicago, Chicago, IL, USA

²Committee on Development, Regeneration, and Stem Cell Biology, University of Chicago, Chicago, IL, USA

³Institute for Biophysical Dynamics, University of Chicago, Chicago, IL, USA

29 arranged in a continuous, topologically closed monolayer epithelium that forms the outer cell layer of the ellip-
30 soidal egg chamber—the organ-like structure that gives rise to the egg⁸ (Fig. 1). The apical surfaces of follicle cells
31 adhere to a central germ cell cluster, and their basal surfaces face outward and adhere to a surrounding basement
32 membrane extracellular matrix. The follicle cells migrate along this stationary basement membrane, resulting
33 in rotation of the entire cell cluster. As the cells migrate, they secrete additional basement membrane proteins.
34 The coordination of migration with secretion causes the cells to produce a basement membrane structure that
35 channels tissue growth along one axis^{9–12}. Follicle cell migration lasts for roughly two days, and the migration
36 direction—and resulting direction of egg chamber rotation—is stable throughout¹³. The edgeless geometry of
37 the epithelium means cells are not partitioned into “leader” and “follower” roles, and there is no open space,
38 chemical gradient, or other external guidance cue to dictate the migration direction. Instead, this feat of stable
39 cell polarization and directed migration is accomplished through local interactions between the migrating cells
40 themselves^{14,15}.

41 Follicle cell migration is driven, in part, by lamellipodial protrusions that extend from the leading edge of each
42 cell^{9,16}. Lamellipodia are built by the WASP family verprolin homolog regulatory complex (WAVE complex)^{17,18},
43 which is a protein assembly composed of five subunits: SCAR/WAVE, Abi, Sra1/Cyfp, Hem/Nap1, and HSPC300¹⁹.
44 The WAVE complex adds branches to actin filaments by activating the Actin-related proteins-2/3 complex (Arp2/3)
45 and elongates existing filaments, building the branched actin network that pushes the leading edge forward^{20–22}.

46 The follicle cells align their lamellipodial protrusions across the tissue, a form of planar polarity^{9,16}. The atypical
47 cadherin Fat2 is required for both planar polarity and collective migration to occur^{23,24}. Fat2 is polarized to
48 the trailing edge of each cell²⁴, where it promotes the formation of protrusions at the leading edge of the cell
49 behind¹⁴. Interestingly, in addition to migration depending on polarized Fat2 activity, Fat2’s planar polarity also
50 depends on epithelial migration¹⁴. It is not known how Fat2 regulates lamellipodia or cell polarity, or how these
51 processes influence one another. We hypothesized that Fat2 acts as a coupler between tissue planar polarity and cell
52 protrusion by polarizing WAVE complex activity to the leading edge. To test this, we used genetic mosaic analysis
53 and quantitative imaging of fixed and live tissues to dissect Fat2’s contributions to protrusivity and protrusion
54 polarity at cell and tissue scales.

55 We show that Fat2 signals in *trans*, entraining WAVE complex activity to one long-lived region along each leading
56 edge. Without Fat2, the WAVE complex accumulates and dissipates at different regions around the cell perime-
57 ter, and cell protrusivity is reduced and unpolarized. Without stable polarization of protrusions within cells or
58 across the epithelium, collective cell migration fails. The interaction between Fat2 and the WAVE complex is
59 non-cell-autonomous but quite local, with sub-micron-scale puncta of Fat2 along the trailing edge concentrating
60 the WAVE complex just across the cell-cell interface, at the tips of filopodia embedded within the lamellipodium.
61 These findings demonstrate how an intercellular interaction between Fat2 and the WAVE complex increases cell
62 protrusivity, stabilizes regions of protrusive activity along the cell perimeter, and aligns protrusions across the
63 epithelium by coupling leading and trailing edges. Fat2-WAVE complex interaction thereby stabilizes the planar
64 polarity of protrusions for directionally persistent collective migration.

65 Results

66 **Fat2 increases and polarizes protrusions at the basal surface of the follicular epithelium**

67 Recent work has shown that Fat2 regulates migration of the follicular epithelium by polarizing F-actin-rich pro-
68 trusions; specifically, Fat2 in a given cell causes protrusions to form at the leading edge of the cell behind it, and
69 without Fat2, protrusions are reduced or lost^{14,25}. Beyond this qualitative description, it is not known how Fat2
70 modulates cell protrusion. Because protrusion is a dynamic process of spatially coordinated cell extension and
71 retraction, we used live imaging and fluorescent labeling of the plasma membrane to obtain a more detailed, time-
72 resolved view of protrusions and their distribution around cells. We acquired timelapses of the basal surface of
73 control and *fat2*^{N103-2} epithelia (a null allele, hereafter referred to as *fat2*). There was substantial protrusive ac-
74 tivity in *fat2* epithelia, but these protrusions lacked the clear polarized distribution of control epithelia (Fig. 2A;
75 Movie 1).

76 To quantify the extent and distribution of protrusion in these data, we developed methods to segment mem-
77 brane extensions and measure their lengths and orientations (Fig. S1). We briefly summarize our quantification
78 approach here; we include a more detailed explanation in the Methods and Materials. First, we measured the
79 lengths of membrane extensions from all cell-cell interfaces (Fig. 2B). The distribution of measured lengths was
80 unimodal, with no natural division between protrusive and non-protrusive interfaces. Therefore, to establish an
81 empirically-grounded cutoff between these categories, we recorded timelapses of control epithelia treated with the
82 Arp2/3 inhibitor CK-666, which are non-migratory and almost entirely non-protrusive. We used measurements
83 from CK-666-treated epithelia to set a cutoff for the minimum length of a protrusion: any edges with membrane
84 extensions longer than the 98th percentile of those in CK-666-treated epithelia were considered *protrusive* for
85 subsequent analysis.

86 It has been shown that Fat2 regulates follicle cell protrusivity and planar polarity^{14,23,25}, but it is not understood
87 how these aspects of its function relate to one another. To address this, we measured the changes in the extent
88 and polarity of protrusions that resulted from a loss of Fat2. We found that both control and *fat2* epithelia were
89 more protrusive than CK-666-treated epithelia. The protrusivity of *fat2* epithelia was lower than that of control
90 on average, but highly variable, with overlap between the protrusivity distributions of both untreated and CK-
91 666-treated epithelia (Fig. 2B,C; S2A; Movie 1). As a complementary method, we also measured protrusivity via
92 F-actin labeling in fixed tissues, using *abi*-RNAi-expressing epithelia as a nearly non-protrusive benchmark. The
93 results largely paralleled those seen with membrane labeling (Fig. S3A-D; Movie 3); however, with F-actin labeling
94 we measured a larger disparity in protrusivity between *fat2* and control epithelia (Figs. 2C; S3D). Images of
95 follicle cell protrusions visualized by F-actin staining are dominated by fluorescence from filopodia, so the fact that
96 the protrusivity of *fat2* epithelia appears lower in our F-actin measurement than our membrane measurement
97 may indicate that filopodia are disproportionately reduced by loss of Fat2. Altogether, these data show that *fat2*
98 epithelia are less protrusive than control, but do retain some protrusive activity.

99 These results raised a question: If some *fat2* epithelia have levels of membrane protrusivity comparable to that
100 of control epithelia, then why do all *fat2* epithelia fail to migrate^{13,24}? We hypothesized that mis-polarization
101 of protrusions across the epithelium contributes to *fat2* migration failure. In control epithelia, protrusions were

102 most often polarized orthogonally to the egg chamber's anterior-posterior axis, in the direction of migration (Fig.
103 2A,D; S2B; Movie 2). In contrast, in *fat2* epithelia, protrusions were fairly uniformly distributed in all directions
104 or biased in two opposite directions. Where an axial bias was present, the axis was inconsistent between epithelia
105 (Fig. 2A,D; S2B; Movie 2). We also confirmed this finding using F-actin labeling of protrusions. To compare
106 the planar polarity of F-actin protrusions between control and *fat2*, we measured F-actin enrichment at cell-cell
107 interfaces as a function of interface angle. We again saw that protrusions were planar-polarized in control epithelia
108 and unpolarized in *fat2* epithelia (Fig. S3A,E,F). These data show that Fat2 is required to polarize protrusions in
109 a common direction across the epithelium.

110 Fat2 could be required to polarize protrusions locally at the same cell-cell interface, or it could indirectly polarize
111 protrusions by maintaining tissue-wide planar polarity and collective migration. To distinguish between these
112 possibilities, we took advantage of the fact that although *fat2* epithelia cannot migrate, small groups of *fat2* mu-
113 tant cells can be carried along by their neighbors when they are surrounded by non-mutant, migratory cells²⁴. We
114 generated *fat2* mosaic tissues that had sufficiently small fractions of mutant cells that the tissue as a whole still
115 migrated. We found that *fat2* cells were often protrusive, but their protrusions were not polarized in the direction
116 of migration (Fig. S4; Movie 4). This demonstrates that global migration is not sufficient to correctly polarize
117 protrusions in *fat2* cells. Rather, Fat2 is required in the cell immediately ahead of the protruding cell to polarize
118 that cell's protrusions in alignment with the direction of collective migration.

119 **Fat2 increases and polarizes the WAVE complex at the basal surface of the follicular epithelium**

120 Follicle cell protrusions are built by the WAVE complex¹⁶, so we hypothesized that Fat2 polarizes protrusions by
121 polarizing the WAVE complex distribution. To visualize the WAVE complex in living tissue and at normal expres-
122 sion levels, we used CRISPR/Cas9 to endogenously tag the WAVE complex subunit Sra1 with eGFP (hereafter:
123 Sra1-GFP). We verified that Sra1-GFP is functional by confirming that the flies are viable and fertile as homozy-
124 gotes, Sra1-GFP localizes to follicle cell leading edges like other WAVE complex labels^{16,25}, its localization depends
125 on WAVE complex subunit Abi, and F-actin protrusions appear normal (Fig. S5A-C). Migration was slower
126 when Sra1-GFP was present in two copies (Fig. S5D; Movie 5), so we performed all subsequent experiments
127 with one copy of Sra1-GFP.

128 With an endogenous WAVE complex label in hand, we investigated how Fat2 affects WAVE complex localization.
129 Previous work has shown that WAVE complex levels are reduced at the basal surface of follicle cells lacking Fat2²⁵.
130 Consistent with this result, we found that Sra1-GFP levels were lower at cell-cell interfaces at the basal surface
131 of *fat2* epithelia than of control epithelia (Fig. S6A-C). Planar polarity of Sra1-GFP across the epithelium was
132 also lost in the absence of Fat2 (Fig. S6D,E). Fat2 promotes protrusion in the cell behind, so we next tested the
133 hypothesis that Fat2 localizes the WAVE complex to the leading edge in the same non-cell-autonomous pattern¹⁴
134 (Fig. 3C). We did this using *fat2* mosaic epithelia, in which we could measure Sra1-GFP levels at leading-trailing
135 interfaces shared by control and *fat2* cells. We found that Sra1-GFP levels were normal in *fat2* cells if control
136 cells were present immediately ahead, showing that Sra1 can still localize to the leading edge of cells lacking Fat2.
137 Conversely, Sra1-GFP was reduced at the leading edge of control cells if *fat2* cells were immediately ahead (Fig.
138 3D,E). We conclude that Fat2 non-cell-autonomously localizes the WAVE complex to leading edges, resulting in

139 tissue-wide planar polarization.

140 We wanted to know if loss of the WAVE complex from the leading edge in the absence of Fat2 meant that the
141 protein was redistributed to other cell surfaces. We measured the level of Sra1-GFP at the non-interface basal
142 surface of *fat2* and control cells in *fat2* mosaic epithelia, finding that Sra1-GFP levels were slightly increased in *fat2*
143 cells compared to control cells in the same tissue (Fig. 3D,F). Performing the same measurement in entirely *fat2*
144 or control tissue, there was not a statistically significant increase in Sra1-GFP at the non-interface basal surface,
145 though the trend was the same (Fig. S6C). These data demonstrate that Fat2 concentrates the WAVE complex at
146 the leading edge, and that without Fat2, the WAVE complex becomes distributed more broadly across the basal
147 surface.

148 **Fat2 stabilizes a region of WAVE complex enrichment and protrusivity in *trans***

149 In individually migrating cells, the excitable dynamics of the WAVE complex and its regulators enable it to form
150 transient zones of enrichment along the cell perimeter even in the absence of a directional signal^{7,26,27}. Although
151 the planar polarization of the WAVE complex across the epithelium was lost in *fat2* mutant tissue, we wanted to
152 know (1) whether the WAVE complex could still form regions of enrichment in individual cells and (2) whether
153 these WAVE complex-enriched regions were active and responsible for templating unpolarized protrusions. To
154 evaluate the WAVE complex distribution along the edges of individual cells, we generated entirely *fat2* mutant ep-
155 ithelia in which patches of cells expressed Sra1-GFP. At cell-cell interfaces along Sra1-GFP expression boundaries,
156 we can assess the distribution of Sra1-GFP contributed by one cell. We examined fixed tissues, and found that
157 some boundary interfaces had no enrichment, whereas others had Sra1-GFP enrichment at similar levels to in-
158 terfaces shared by two Sra1-GFP cells. These data show that the WAVE complex can form regions of enrichment
159 without Fat2. Sra1-GFP enrichment coincided with the presence of F-actin protrusions (Fig. 4A), indicating
160 that the WAVE complex in these regions is active. To confirm that the WAVE complex builds the protrusions
161 in *fat2* epithelia, we co-imaged Sra1-GFP and a membrane label, finding that Sra1-GFP was enriched at the tips
162 of membrane protrusions in both control and *fat2* epithelia (Fig. S7A; Movie 6). These data indicate that the
163 WAVE complex can still accumulate and build protrusions in the absence of Fat2, tissue-wide planar polarity, and
164 collective cell migration.

165 A striking feature of migrating follicle cells is the stable polarization of their protrusive leading edge. It is not
166 known whether Fat2 contributes to the stabilization of protrusive regions in addition to its role positioning them.
167 If so, we would expect the protrusive regions of *fat2* epithelia to fluctuate more than those of control epithe-
168 lia, in addition to being less well-polarized. To see if this was the case, we acquired timelapses of Sra1-GFP and
169 monitored the Sra1-GFP distribution along cell perimeters over time. In control epithelia, Sra1-GFP was strongly
170 enriched along leading-trailing interfaces relative to side interfaces over the 20-minute timelapse. Side interfaces
171 were mostly devoid of Sra1-GFP, and punctuated sporadically by Sra1-GFP accumulations that persisted for sev-
172 eral minutes (Fig. 4B-D; Movies 7,8). In contrast, in *fat2* epithelia, the regions of greatest Sra1-GFP enrichment
173 along the cell perimeter changed substantially over the 20-minute timelapse. Multiple Sra1-GFP-enriched regions
174 were often present simultaneously in individual *fat2* cells. The duration of Sra1-GFP accumulation at a given in-
175 terface in *fat2* cells was comparable to the duration of transient Sra1-GFP side accumulation in control cells (Fig.

176 4B-D; Movies 7,8). Because these are both contexts without Fat2, the similar duration of WAVE complex ac-
177 cumulation at these sites suggests a several-minutes timescale over which regions of WAVE complex enrichment
178 can persist without stabilization by Fat2. Similarly, in timelapses with plasma membrane labeled, we observed
179 reduced stability of protrusive regions in control and *fat2* epithelia. In control epithelia, protrusions periodically
180 extended and retracted from one leading edge region, and changes to the direction of cell protrusion were rare
181 (Fig. 4E; Movie 9). In contrast, the protrusive edges of *fat2* cells often shifted substantially over the 20 minutes
182 of the timelapse. Together, these observations show that in addition to polarizing protrusive activity to the lead-
183 ing edge, Fat2 stabilizes the distribution of WAVE complex activity for repeated cycles of protrusion from one
184 long-lived protrusive region.

185 **Fat2 and the WAVE complex colocalize across leading-trailing cell-cell interfaces**

186 It is not known how Fat2 recruits the WAVE complex across the cell-cell interface. In order to constrain the set
187 of possible mechanisms, we assessed the spatial scale of their interaction. Fat2 has a punctate distribution along
188 each cell's trailing edge^{14,24}, so we asked whether Fat2 recruits the WAVE complex locally to these sites, or whether
189 Fat2 more broadly recruits the WAVE complex to the entire interface. We measured the colocalization between
190 Fat2 and the WAVE complex, visualizing Fat2 with an endogenous 3xGFP tag (Fat2-3xGFP) and the WAVE
191 complex with mCherry-tagged Abi under control of the ubiquitin promoter (Abi-mCherry). Like Fat2-3xGFP,
192 Abi-mCherry formed puncta, and Abi-mCherry and Fat2-3xGFP puncta colocalized significantly more than
193 Abi-mCherry and uniformly-distributed E-cadherin-GFP (Spearman's $r = 0.71 \pm 0.04$ vs. 0.49 ± 0.07). Timelapse
194 imaging showed Fat2-3xGFP and Abi-mCherry puncta moving together through cycles of protrusion extension
195 and retraction (Figs. 5A-E; S8A,B; Movie 11). These findings suggest that Fat2 and the WAVE complex interact
196 locally, at the scale of individual puncta.

197 To see whether puncta of Fat2 and the WAVE complex are in fact local sites of WAVE complex recruitment, we
198 investigated whether the distribution of Fat2 puncta controls the distribution of the WAVE complex. To do
199 this, we used an endogenous Fat2 truncation that lacks the intracellular domain (Fat2 Δ ICD-3xGFP), which dis-
200 tributes more broadly around the cell perimeter than wild-type Fat2^{14,28}. We measured the colocalization between
201 Fat2 Δ ICD-3xGFP and Abi-mCherry, finding that they colocalized just as well as Fat2-3xGFP and Abi-mCherry
202 (Spearman's $r = 0.71 \pm 0.04$ vs. 0.71 ± 0.05 , Fig. 5E). From these data we conclude that Fat2 locally controls the
203 distribution of the WAVE complex, with Fat2 puncta concentrating the WAVE complex in corresponding puncta.
204 These findings also demonstrate that the Fat2 intracellular domain is dispensable for Fat2-WAVE complex inter-
205 action. We note that short-lived Abi-mCherry accumulations occasionally formed at cell sides away from Fat2,
206 similar to the Sra1-GFP side accumulations we described previously (Figs. 4D; S9; Movies 7;12). We interpret
207 these as regions of WAVE complex enrichment that had "escaped" Fat2-dependent concentration at the leading
208 edge.

209 It is unknown if there are functional consequences of the punctate organization of Fat2 or the WAVE complex.
210 We hypothesized that other structures localized by Fat2-WAVE complex puncta would have a similar distribution,
211 so we next characterized the spatial context of Fat2-WAVE complex puncta with respect to other known compo-
212 nents of the leading edge. Filopodia, which are built by the actin elongation factor Ena, are embedded within and

213 grow from lamellipodia along the leading edge^{16,29}. Labeling of filopodia tips using a GFP-tagged Ena transgene
214 (GFP-Ena) revealed that the sites of highest Fat2-3xGFP and Abi-mCherry enrichment coincided with filopodia
215 tips (Figs. 5C,D,F; S8C,D). Fluorescence intensity profiles along filopodia lengths showed that Fat2-3xGFP and
216 Abi-mCherry were enriched just ahead of the F-actin-rich region (Fig. 5F,G). Fat2-3xGFP was shifted slightly
217 forward from Abi-mCherry, consistent with the separation of Fat2-3xGFP and Abi-mCherry fluorophores by a
218 cell-cell interface (Figs. 5F,G; S8D,E). This analysis demonstrates a stereotyped organization in which Fat2 and
219 the WAVE complex are concentrated along with Ena near the tips of the filopodia, with Fat2 at the trailing edge
220 across the cell-cell interface from the leading edge components.

221 The close spatial relationship between Fat2, the WAVE complex, and filopodia tips suggests that the positions
222 of Fat2 and WAVE complex puncta determine the position of filopodia. However, an alternative possibility is
223 that the filopodia mediate colocalization between Fat2 and the WAVE complex. To test this latter hypothesis,
224 we measured colocalization between Fat2-3xGFP and Abi-mCherry in *ena*-RNAi-expressing epithelia, in which
225 filopodia are strongly depleted and the underlying lamellipodial actin network is revealed¹⁶ (Fig. S8F). Despite
226 the loss of filopodia, there was only a slight reduction in Fat2-3xGFP-Abi-mCherry colocalization (Spearman's
227 $r = 0.71 \pm 0.04$ vs. 0.65 ± 0.03 , Fig. S8A,B). We therefore rule out Ena or the filopodia themselves as required
228 mediators of the spatial relationship between Fat2 and the WAVE complex, and infer that Ena's colocalization
229 with Fat2 and the growth of filopodia from these sites are secondary consequences of the Fat2-WAVE complex
230 interaction. We propose that Fat2 puncta position WAVE complex puncta, which in turn position filopodia
231 along the leading edge.

232 A cell membrane separates Fat2 and WAVE complex puncta, so we hypothesized that a transmembrane receptor at
233 leading edges mediates Fat2's recruitment of the WAVE complex. Like the WAVE complex, the receptor tyrosine
234 phosphatase Lar is recruited to the leading edge by Fat2, where it promotes protrusion^{14,25}. To test the hypothesis
235 that Fat2's recruitment of the WAVE complex is mediated by Lar, we measured colocalization between Fat2-
236 3xGFP and Abi-mCherry in epithelia in which functional Lar is absent from follicle cells (*lar*^{13.2}/*lar*^{bola1}, referred
237 to as *lar*)^{30,31}. The amount of Abi-mCherry along cell-cell interfaces was reduced by ~25% in this background
238 (Fig. S8G), consistent with previous findings²⁵, but colocalization between the remaining Abi-mCherry and
239 Fat2-3xGFP was not significantly reduced (Spearman's $r = 0.71 \pm 0.04$ vs. 0.68 ± 0.03 , Fig. S8A,B). We conclude
240 that while Lar shapes the WAVE complex distribution in some way, it is not the sole molecular bridge between
241 Fat2 and the WAVE complex.

242 Altogether, we propose that Fat2 acts locally, at the scale of individual Fat2 puncta, to concentrate the WAVE
243 complex in corresponding puncta across the cell-cell interface. Because Fat2 puncta are distributed along the
244 trailing edge, this has the broader effect of stabilizing a region of WAVE complex enrichment at the leading edge.

245 Discussion

246 This work demonstrates that a *trans* interaction between the atypical cadherin Fat2 and the WAVE complex can
247 stabilize WAVE complex polarity for directed cell migration. Fat2, localized to the trailing edge of each cell, re-
248 cruits the WAVE complex to the leading edge of the cell behind, just across their shared interface. By concentrating

249 WAVE complex activity in a restricted region, Fat2 strongly biases lamellipodia and filopodia to form at these lead-
250 ing edge sites, stably polarizing overall cell protrusive activity to one cell side. Because the Fat2-WAVE complex
251 signaling system is deployed at each leading-trailing interface in a planar-polarized manner, it both polarizes pro-
252 trusions within individual cells and couples these individual cell polarities across the epithelium. This allows the
253 cells to exert force in a common direction and achieve a highly coordinated collective cell migration.

254 While the molecular players differ, local coupling of leading and trailing edges through asymmetric transmem-
255 brane cues has been a recurring motif in studies of epithelial and endothelial collective cell migrations. In an
256 epithelial cell culture model of collective migration, asymmetric pulling forces across cell-cell interfaces polarize
257 Rac1 activity and cell protrusion³². In another model, one cell's lamellipodium is stabilized by confinement un-
258 der the trailing edge of the cell ahead, reinforcing interface asymmetry³³. In an endothelial collective cell migration
259 model, asymmetric membrane “fingers” containing VE-cadherin extend from the trailing edge and are engulfed
260 by the leading edge of the cell behind, whose movement they help guide³⁴. These types of leading-trailing edge
261 coupling systems could operate together with longer-range cues to reinforce the planar polarity of cells' migratory
262 structures. In migrations with a closed topology and no extrinsic directional cues, such as that of the follicle cells,
263 local polarity coupling may be especially critical for collective migration.

264 We were able to come to a more detailed understanding of cell-cell coupling and of Fat2's role in follicle cell
265 collective migration by developing new computational tools to automatically identify and measure membrane
266 protrusions. Applying these tools to timelapses of epithelia with a live membrane label revealed that Fat2 has a
267 pronounced effect on the orientation of protrusive activity as well as its extent. Even in the context of a globally
268 planar-polarized, migratory epithelium, cells without input from Fat2 in the cell ahead are unable to polarize their
269 protrusions in the direction of migration. Although we focused on the length and orientation of protrusions in
270 this study, this approach could be extended to other protrusion traits such as shape, lifetime, or elongation rate,
271 and/or to other tissues, making it broadly applicable to studies of collective migrations of epithelial cells.

272 The misoriented protrusions in *fat2* epithelia exhibited excitable WAVE complex dynamics similar to those de-
273 scribed in other systems^{26,35,36}. We also saw hallmarks of WAVE complex excitability in the protrusions that occur
274 at low frequencies in wild-type cells along side-facing interfaces (i.e. those at which Fat2 is not enriched on either
275 side of interface). In both cases, the WAVE complex accumulated at an edge region, spread outward along the
276 membrane, and then dissipated. This corresponded with the initiation, growth, and collapse of a protrusion.
277 Where Fat2 was present, WAVE complex distribution along the cell perimeter stayed more constant, although
278 at the puncta scale it may have been undergoing cycles of accumulation and dissipation in-place. In addition to
279 forming shorter-lived regions of enrichment without Fat2, the WAVE complex distributed more broadly across
280 the plasma membrane. We propose that this caused the reduced protrusion polarity we observed in *fat2* epithe-
281 lia. It could also account for the overall reduced protrusivity of *fat2* epithelia by lowering the frequency with
282 which the WAVE complex crosses the enrichment threshold at which a protrusion is initiated. We interpret the
283 broader WAVE complex distribution in *fat2* epithelia as evidence that, in addition to locally favoring WAVE com-
284 plex accumulation, Fat2 may sequester enough WAVE complex to suppress protrusion elsewhere. The sporadic
285 side-facing protrusions in wild-type cells show that the Fat2 signaling system does not exert perfect control over
286 the distribution of WAVE complex activity, but this level of control is sufficient to stably polarize cell protrusive

287 activity for days-long, highly directed migration.

288 Given that the WAVE complex is capable of local excitation and the initiation of protrusions without Fat2, then
289 what is the mechanistic basis for how Fat2 shapes the WAVE complex's distribution and dynamics in wild-type
290 cells? The WAVE complex is activated by recruitment to the plasma membrane^{19,37,38}. Positive regulators of
291 WAVE complex accumulation include active Rac, phosphatidylinositol (3,4,5)-triphosphate (PIP₃), membrane-
292 localized proteins that directly bind the WAVE complex, and the WAVE complex itself^{17,36,37,39–43}. We hypothe-
293 size that Fat2 promotes WAVE complex accumulation within a stable region by modulating one or more of these
294 inputs, thereby controlling the site where the WAVE complex excitation threshold is crossed and a protrusion is
295 formed. Under this model, in the absence of Fat2, this site selection instead becomes more stochastic and there-
296 fore long-lasting protrusive regions cannot form. Fat2 and the WAVE complex interact *in trans* and cannot be in
297 direct physical contact, so we expect that part of this signaling system is a transmembrane protein at the leading
298 edge. We investigated Lar as a candidate for this role, but found that loss of Lar alone does not fully disrupt Fat2-
299 WAVE complex colocalization. Lar therefore likely acts along with one or more other transmembrane proteins to
300 concentrate the WAVE complex at the leading edge. In future work, it will be particularly informative to identify
301 the Fat2 binding partner or other molecules that participate on the leading edge side of this signaling system.

302 Fat2 is localized in puncta along the trailing edge^{14,24}, and we show here that those puncta correspond 1:1 with
303 regions of high WAVE complex enrichment and filopodia tips just across the cell-cell interface. Fat2's punctate dis-
304 tribution and its levels along cell-cell interfaces are unaffected by loss of the WAVE complex¹⁴, supporting a model
305 in which Fat2 puncta shape the distribution of the WAVE complex and protrusions, not the reverse. Cadherins
306 are commonly observed organized in puncta, though the causes and functions of this organization vary^{44–46}. For
307 example, Flamingo (or mammalian Celsr1), an atypical cadherin and central component of the core planar cell
308 polarity pathway, is stabilized by clustering, and this clustering is important for its planar polarization^{47–49}. In
309 future work, it will be important to determine how Fat2 assembles in puncta, and whether this localization is
310 important for its polarization to trailing edges or its effect on the organization of leading edges. More broadly, it
311 will be critical to determine how Fat2 achieves its trailing edge localization, a necessary step in the polarization of
312 the tissue.

313 **Author Contributions**

314 A.M.W. and S.H.-B. conceived of the study. A.M.W. designed experiments with critical input from all authors.
315 A.M.W. generated new reagents and performed experiments. A.M.W. and S.D. wrote data analysis software and
316 analyzed data. All authors contributed to data interpretation. A.M.W. prepared figures. A.M.W. and S.H.-B.
317 wrote the manuscript with editorial input from all authors.

318 **Acknowledgements**

319 We thank members of the Horne-Badovinac and Munro labs, Allison Zajac, Sherzod Tokamov, Ellie Heckscher,
320 Michael Glotzer, and Carmen Williams for feedback throughout the study and comments on the manuscript.
321 This work was supported by NIH R01 GM126047 to S.H.B., NIH T32 HD055164 to A.M.W., and University
322 of Chicago Fellows and Jane Coffin Childs Memorial Fund for Medical Research to S.D..

323 **Figures**

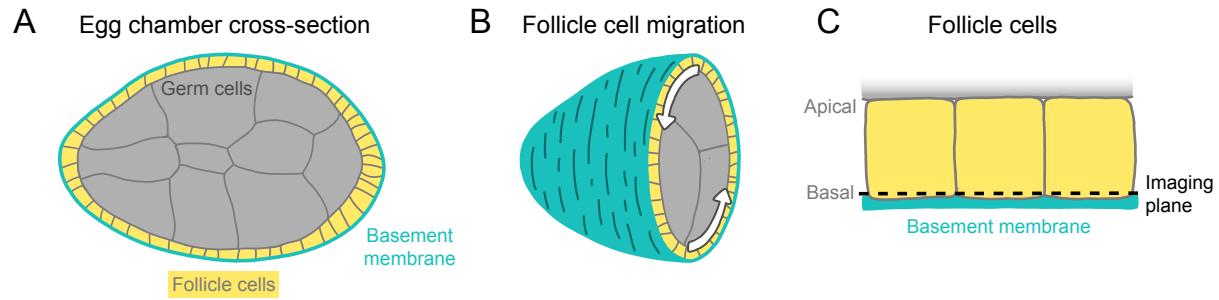


Figure 1: **Introduction to egg chamber rotation.** **A**, Diagram of a stage 6 egg chamber in cross-section. Anterior is left, posterior right. **B**, Three-dimensional diagram of an egg chamber with the anterior half shown. Arrows indicate the migration of follicle cells along the basement membrane and resulting rotation of the egg chamber around its anterior-posterior axis. **C**, Diagram of three follicle cells. Their apical surfaces adhere to the germ cells and their basal surfaces adhere to the basement membrane. The dashed line represents the basal imaging plane used throughout this study except where indicated.

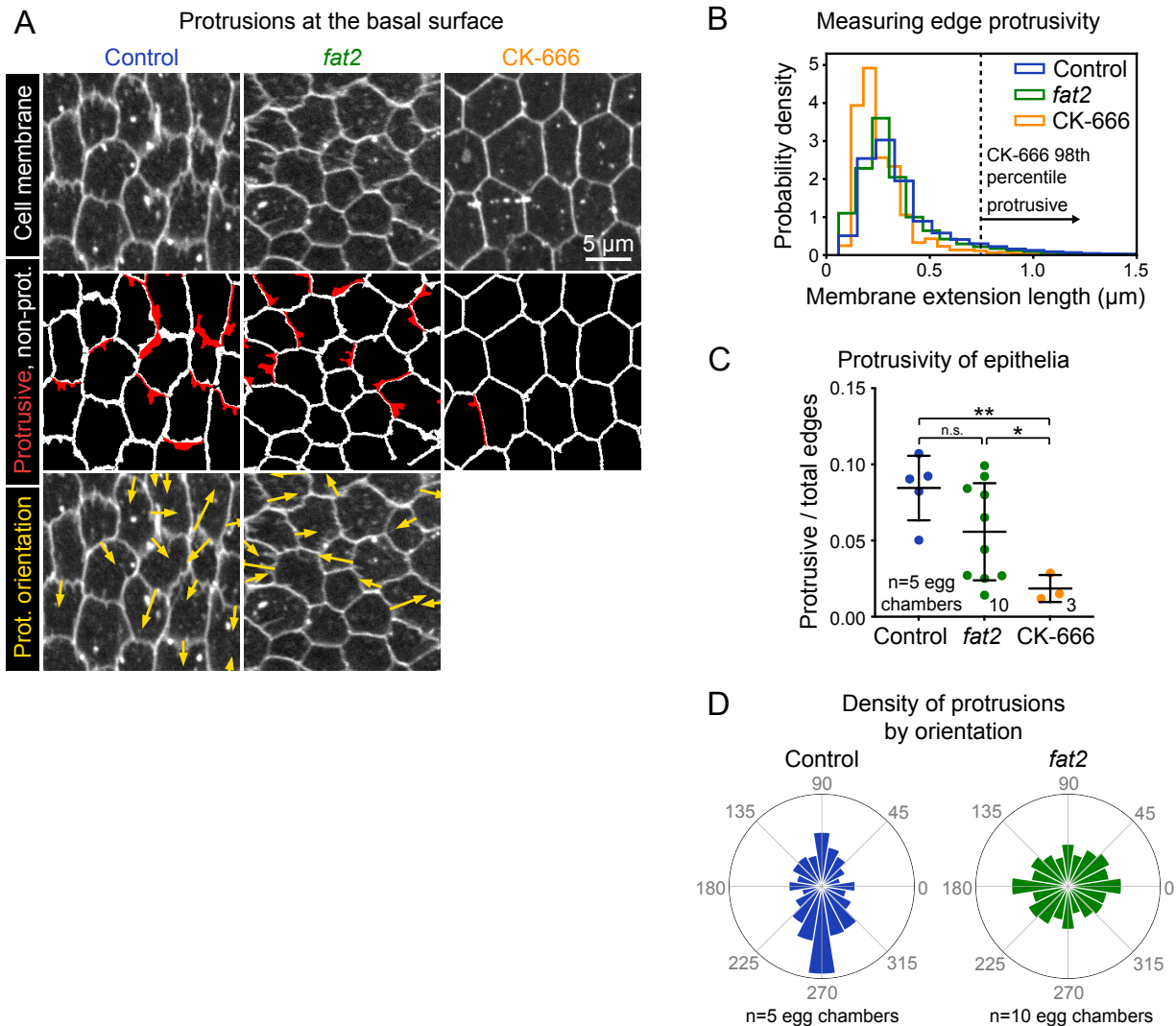


Figure 2: **Fat2 increases and polarizes follicle cell protrusivity.** **A**, Timelapse frames of control, *fat2*, and CK-666-treated epithelia labeled with a membrane dye. Middle row shows segmented edges. Protrusive edges, defined as edges with membrane extensions longer than the 98th percentile of those of CK-666-treated epithelia, are red. Non-protrusive edges are white. Bottom row shows arrows indicating the orientation of each protrusion overlaid on cell membrane. Arrows originate at protrusion bases and have lengths proportional to protrusion lengths. See related Movies 1, 2. **B**, Histogram showing the distribution of edge widths. The 98th percentile width threshold for CK-666-treated epithelia is indicated. **C**, Plot showing the ratio of protrusive to total edges. The protrusivity of *fat2* epithelia is variable, with a distribution overlapping with control and CK-666-treated epithelia. Welch's ANOVA ($W(2,8.75)=19.3, p=0.0006$) with Dunnett's T3 multiple comparisons test; n.s. $p=0.16$, * $p=0.021$, ** $p=0.0024$. **D**, Polar histograms of the distribution of protrusion orientations in control and *fat2* epithelia. Anterior is left, posterior is right, and in control epithelia images were flipped as needed so that migration is downward. Control protrusions point predominantly in the direction of migration, whereas *fat2* protrusions are less polarized. Associated with Figs. S1, S2, S3, S4; Movies 1, 2, 3, 4.

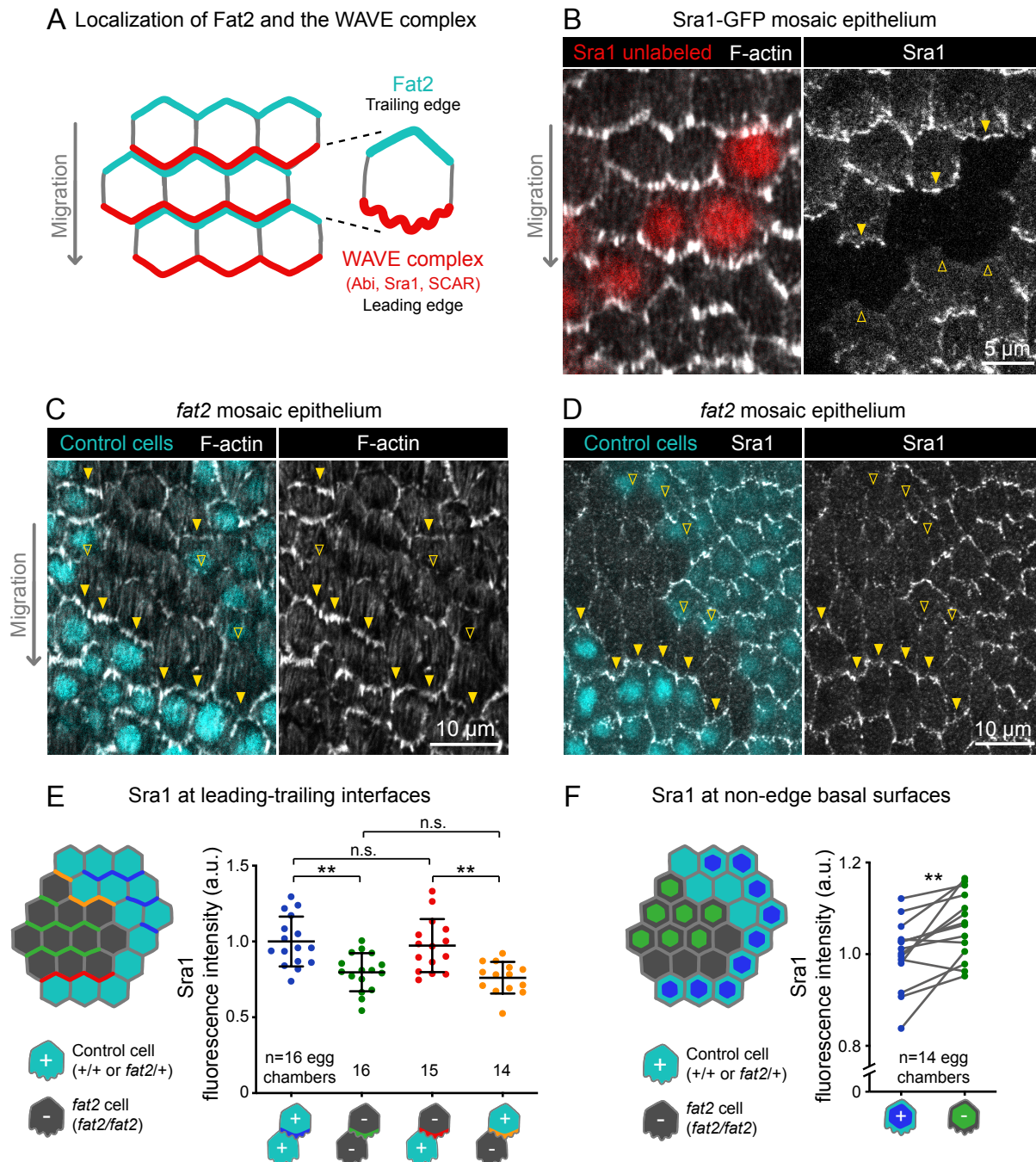


Figure 3: Fat2 concentrates the WAVE complex at the leading edge of the cell behind. **A**, Diagram showing Fat2 localization at the trailing edge and WAVE complex at the leading edge of the basal surface of follicle cells, with WAVE complex subunits referenced in this paper listed. **B**, Images of an Sra1-GFP mosaic epithelium with phalloidin-stained F-actin, showing Sra1-GFP enrichment at leading edges (filled arrows) and not trailing edges (open arrows). **C**, Images of a *fat2* mosaic epithelium with phalloidin-stained F-actin. Filled arrows indicate leading edges of *fat2* cells behind control cells, where protrusions are present. Open arrows indicate leading edges of control cells behind *fat2* cells, where protrusions are reduced. **D**, Images of a *fat2* mosaic epithelium expressing Sra1-GFP. Filled arrows indicate leading edges of *fat2* cells behind control cells. Open arrows indicate leading edges of control cells behind *fat2* cells. **E,F**, Quantification of Sra1-GFP mean fluorescence intensity in *fat2* mosaic epithelia along leading-trailing interfaces (**E**) or non-interface basal surfaces (**F**). Diagrams to the left of plots show the measured regions with respect to control (cyan) and *fat2* (gray) cells. The genotype(s) of cells in each measured category are shown below the X axis. **E**, Sra1-GFP is reduced at the leading edge of cells of any genotype behind *fat2* cells. Bars indicate mean \pm SD. One-way ANOVA ($F(3,57)=10.40$, $p<0.0001$) with post-hoc Tukey's test; n.s. (left to right) $p=0.96$, 0.90 , $**p<0.01$. **F**, Sra1-GFP is slightly increased at the non-interface basal surface of *fat2* cells. Lines connect measurements from the same egg chamber. Paired t-test; $**p<0.01$. Associated with Figs. S5, S6; Movie 5.

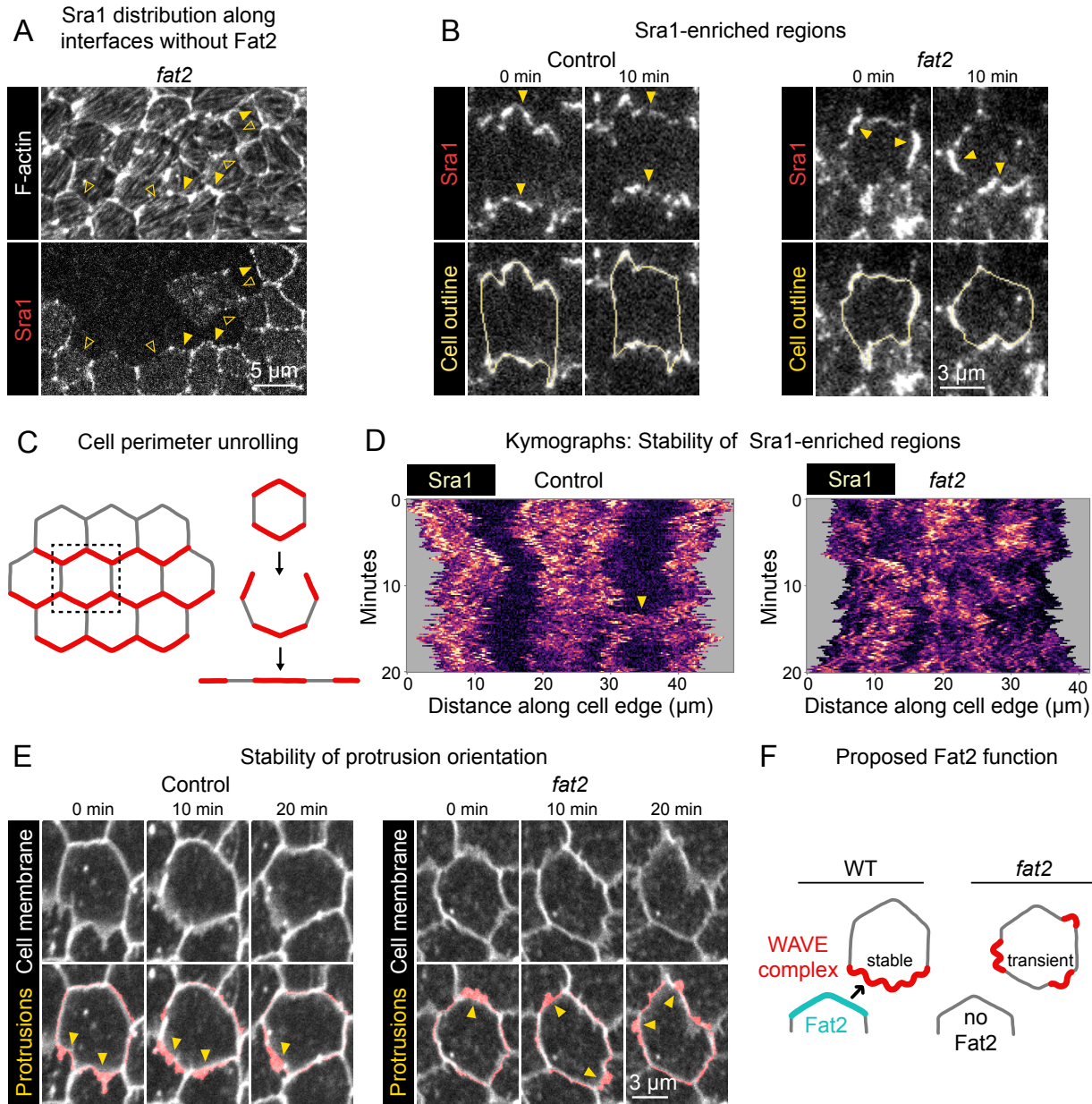


Figure 4: Fat2 stabilizes a region of WAVE complex enrichment and protrusivity. **A**, Images of phalloidin-stained F-actin and mosaically-expressed Sra1-GFP in an entirely *fat2* mutant epithelium. Filled and open arrows indicate genotype boundary interfaces with and without Sra1-GFP enrichment, respectively. Sra1-GFP enrichment is heterogeneous, and interfaces with Sra1-GFP enrichment have more F-actin protrusions. **B**, Timelapse frames of Sra1-GFP in control and *fat2* epithelia. Top row shows Sra1-GFP with arrows indicating regions of Sra1-GFP enrichment; bottom row shows Sra1-GFP and outlines of cell perimeters used to make kymographs. Laser intensity and brightness display settings differ between genotypes. See related Movies 7, 8. **C**, Diagram of cell perimeter unrolling for kymograph generation. Red represents planar-polarized Sra1 as distributed before and after unrolling. **D**, Kymographs of Sra1-GFP fluorescence intensity along cell perimeter outlines exemplified in (C). The Y-axis length of regions of high Sra1-GFP enrichment reports their stability over time. Control cells have Sra1-GFP regions along leading-trailing interfaces that are stable over 20 minutes. In *fat2* cells, Sra1-GFP-enriched regions are less stable. The arrow indicates a transient accumulation of Sra1-GFP at a control cell side. These occur occasionally, and their stability is similar to Sra1-GFP regions in *fat2* cells. **E**, Timelapse frames of control and *fat2* epithelia with a membrane dye. Top row shows the interfaces and protrusions of one cell and its neighbors. Segmented membrane extensions originating from the center cell (red) are overlaid in the bottom row. Arrows indicate sites of membrane protrusion. The position of protrusions in the *fat2* cell changes more than in the control cell. See related movie 9. **F**, Diagram showing the proposed role of Fat2 stabilizing a region of WAVE complex enrichment and protrusivity. Without Fat2, WAVE complex-enriched, protrusive regions are reduced and more transient. Associated with Fig. S7; Movies 6, 7, 8, 9, 10.

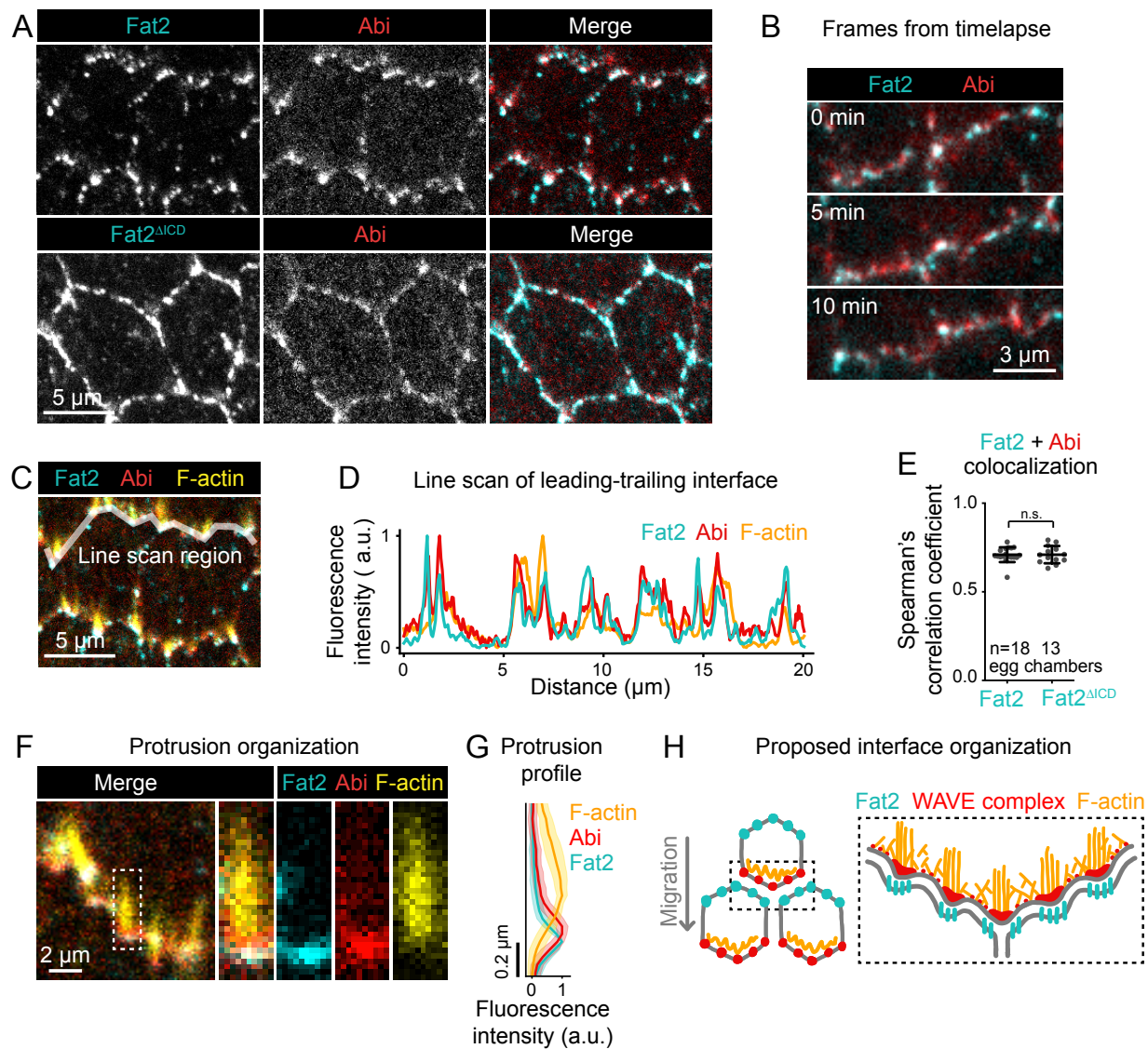


Figure 5: Fat2 colocalizes with the WAVE complex across leading-trailing cell-cell interfaces. **A**, Images of cells expressing Abi-mCherry and endogenous full-length Fat2-3xGFP or endogenous Fat2-3xGFP lacking the intracellular domain (Fat2^{ΔICD}), used to assess colocalization. **B**, Timelapse frames showing the leading-trailing interfaces of two cells expressing Fat2-3xGFP and Abi-mCherry, showing their colocalization over time. See related Movie 11. **C**, Image showing the leading-trailing interface region used in (D) and example of a region used in (E). **D**, Line scan showing the fluorescence intensity of Fat2-3xGFP, Abi-mCherry, and F-actin (phalloidin) along the leading-trailing interfaces of the two cells in (D), showing their corresponding peaks of enrichment. **E**, Plot of Spearman's correlation coefficients of Fat2-3xGFP or Fat2^{ΔICD}-3xGFP and Abi-mCherry showing no significant difference in colocalization. Bars indicate mean ± SD. One-way ANOVA ($F(4,69)=52.96$, $p<0.0001$) with post-hoc Tukey's test; n.s. $p>0.9999$. **F**, Image showing the distribution of Fat2-3xGFP, Abi-mCherry, and F-actin (phalloidin) at the leading-trailing interface and along the boxed filopodium. **G**, Plot showing fluorescence intensity of traces of F-actin, Abi-mCherry, and Fat2-3xGFP showing their relative sites of enrichment along the length of filopodia. Lines and shaded regions indicate mean ± SD. $n=74$ protrusions (used for SD), 18 cells, 1 cell/egg chamber. **H**, Diagram of hypothesized organization of Fat2, the WAVE complex, and F-actin along the leading-trailing interface based on the present data and previously published work^{14,16,24}. Fat2 puncta at the trailing edge colocalize with WAVE complex puncta at the leading edge, ahead of filopodia embedded within the lamellipodium. Associated with Figs. S8, S9; Movies 11, 12.

324 **Methods and Materials**

325 **Materials, data, and code availability**

326 New plasmids and *Drosophila* lines reported in this paper are available upon request to the corresponding author,
327 as are all datasets and the code necessary to reproduce our analyses.

328 ***Drosophila* sources, care, and genetics**

329 The sources and references of all stocks used in this study are listed in Supplemental Table 1 and the genotypes of
330 *Drosophila* used in each experiment and associated figure panels are listed in Supplemental Table 2. *Drosophila*
331 were raised at 25°C and fed cornmeal molasses agar food. Females 0-3 days post-eclosion were aged on yeast with
332 males prior to dissection. In most cases, they were aged for 2-3 days at 25°C. Temperatures and yeasting times used
333 for each experiment are reported in Supplemental Table 3. In all RNAi experiments, *traffic jam*>Gal4 (*tj*>Gal4)⁵⁰
334 was used to drive RNAi expression in follicle cells and not in germ cells. Sra1-GFP and *fat2* mosaic epithelia were
335 generated using the Flp/FRT method^{51,52}, using FRT82B and FRT80B recombination sites, respectively. In both
336 cases *tj*>Gal4 was used to drive expression of UAS>Flp recombinase.

337 **Generation of Sra1-GFP**

338 Endogenous Sra1 was tagged C-terminally with enhanced GFP (GFP) following the general approaches described
339 by Gratz *et al.* (2013) and Gratz *et al.* (2014)^{53,54}. The guide RNA target sequence 5'-GCTTAAATGCATCC
340 CTT[†]TCCGGG-3' was chosen with flyCRISPR Target Finder⁵⁴. The underlined sequence was cloned into the
341 pU6-BbsI-chiRNA plasmid, and the bold sequence is the adjacent PAM motif. For homologous recombination,
342 homology arms approximately 2 kb long flanking the insertion target site were amplified from genomic DNA
343 from the y1 M{nos-Cas9.P}ZH-2A w* (nanos-Cas9)⁵⁵ background. GFP was amplified from the pTWG plas-
344 mid. A linker with sequence encoding the amino acids 'GSGGSGGS' was added to the N-terminal side of GFP.
345 Homology arms, linker, and GFP were inserted into donor plasmid pDsRed-attP, which contains 3xP3-DsRed
346 flanked by loxP sites for insertion screening and subsequent removal. The linker-GFP insertion was made imme-
347 diately before the Sra1 stop codon. Guide and homologous recombination plasmids were injected by Genetivi-
348 sion Inc. into the nanos-Cas9 background. F1 males were screened for 3xP3-DsRed and then 3xP3-DsRed was
349 excised by crossing to Cre-expressing flies (MKRS hsFLP/TM6b Cre).

350 **Egg chamber dissection**

351 Ovaries were dissected into live imaging media (Schneider's *Drosophila* medium with 15% fetal bovine serum and
352 200 µg/mL insulin) in a spot plate using 1 set of Dumont #55 forceps and 1 set of Dumont #5 forceps. Ovarioles
353 were removed from the ovary and from ovariole muscle sheathes with forceps. For live imaging, egg chambers
354 older than the egg chamber to be imaged were removed from the ovariole strands by cutting through the stalk
355 with a 27-gauge hypodermic needle. For fixed imaging, egg chambers older than stage 9 were removed prior
356 to fixation. Removal of older egg chambers allows more compression of the imaged egg chamber between the
357 slide and coverslip so that the basal surface of a field of cells can be imaged in a single plane. For a more detailed
358 description and movies of dissection, see Cetera *et al.* (2016)⁵⁶.

359 **Live imaging sample preparation**

360 Following dissection, ovarioles were transferred to a fresh well of live imaging media. For membrane staining,
361 CellMask Orange or Deep Red plasma membrane stain (Thermo Fisher Scientific, Waltham, MA, 1:500) was
362 added and ovarioles incubated for 15 minutes, followed by a wash in live imaging media to remove excess stain
363 before mounting. Ovarioles were then transferred to a glass slide with 20 μ L of live imaging media. For CK-666
364 treatment, following plasma membrane staining, ovarioles were transferred to live imaging media with 750 μ M
365 CK-666 (Millipore Sigma, St. Louis, MO) and then mounted in the same media. Glass beads with diameter 51
366 μ m were added to support the 22x22 mm #1.5 coverslip and limit egg chamber compression. Coverslip edges
367 were sealed with melted petroleum jelly to prevent evaporation while imaging. Samples were checked for damage
368 using the membrane stain or other fluorescent markers as indicators, and excluded if damage was observed. Slides
369 were used for no more than 1 hour.

370 **Immunostaining and F-actin staining**

371 Following dissection, ovarioles were fixed in 4% EM-grade formaldehyde in PBT (phosphate buffered saline +
372 0.1% Triton X-100) and then washed 3x5 minutes in PBT at room temperature. Egg chambers were incubated
373 with primary antibodies in PBT overnight at 4°C (anti-Scar, 1:200) or for 2 hours at room temperature (anti-
374 Discs Large, 1:20) while rocking. Ovarioles were then washed 3x5 minutes in PBT and incubated in secondary
375 antibody diluted 1:200 in PBT for two hours at room temperature while rocking. F-actin staining was performed
376 using either TRITC phalloidin (Millipore Sigma, 1:250) or Alexa Fluor™ 647 phalloidin (Thermo Fisher Scien-
377 tific, 1:50). If TRITC phalloidin was the only stain or antibody used, it was added directly to the fixation media
378 for 15 minutes of staining concurrent with fixation. Otherwise, TRITC phalloidin was added for 15-30 minutes
379 at room temperature as the final staining step. Alexa Fluor™ 647 phalloidin staining was performed for two
380 hours at room temperature while the sample was rocking, concurrent with secondary antibody staining where
381 applicable. Ovarioles were then washed 3x5 minutes in PBT and mounted in 40 μ L SlowFade Diamond™
382 antifade on a slide using a 22x50 mm #1.5 coverslip, sealed with nail polish, and stored at 4°C until imaged.

383 **Microscopy**

384 **Laser scanning confocal microscopy**

385 Laser scanning confocal microscopy was used for all fixed imaging and for live imaging of membrane-dyed egg
386 chambers. Imaging was performed with a Zeiss LSM 800 upright laser scanning confocal with a 40x/1.3 NA EC
387 Plan-NEOFLUAR oil immersion objective or a 63x/1.4 NA Plan-APOCHROMAT oil immersion objective,
388 diode lasers (405, 488, 561, and 640 nm), and GaAsP detectors. The system was controlled with Zen 2.3 Blue
389 acquisition software (Zeiss). Imaging was performed at room temperature. All images show the basal surface of
390 stage 6-7 egg chambers except for Fig. S5A, bottom row, which shows follicle cells in cross-section. Cross-section
391 images were used for egg chamber staging throughout. Confocal microscopy was used to capture the images in
392 Figs. 2; 3; 4A,E; 5A,C-G; S1; S2; S3A-C,E,F; S4; S5; S6; S7A; S8; Movies 1; 2; 4; 5; 6; 9.

393 **TIRF microscopy**

394 Near-TIRF microscopy was used to visualize Fat2-GFP, Sra1-GFP, Abi-mCherry, and F-Tractin-tdTomato⁵⁷ dy-
395 namics at the basal surface. Near-TIRF imaging was performed with a Nikon ECLIPSE-Ti inverted microscope
396 with Ti-ND6-PFS Perfect Focus Unit, solid-state 50 mW 481 and 561 nm Sapphire lasers (Coherent technology),
397 motorized TIRF illuminator, laser merge module (Spectral Applied Research), Nikon CFI 100x Apo 1.45 NA
398 oil immersion TIRF objective with 1.5x intermediate magnification, and Andor iXon3 897 electron-multiplying
399 charged-coupled device (EM-CCD) camera. Image acquisition was controlled using MetaMorph software. For
400 two color imaging, frames were collected for each color consecutively with the TIRF illumination angle adjusted
401 in between. Imaging was performed at room temperature. Movies were corrected for bleaching using the his-
402 togram matching method in Fiji (ImageJ)^{58,59}. TIRF microscopy was used to capture the images in Figs. 4B,D;
403 5B; S3D; S7B,C; S9; Movies 3; 7; 8; 10; 11.

404 **Cell and protrusion segmentation from timelapses of cell membrane**

405 Protrusions from timelapse datasets of the follicle cell basal surface stained with CellMask Orange (see Live imag-
406 ing sample preparation) were segmented with the Python scikit-image and scipy libraries (Fig. S1)^{60,61}. First, each
407 cell was segmented and tracked, with manual corrections to cell-cell interface placements made using napari⁶².
408 Next, we used a watershed-based approach to segment the regions of high fluorescence intensity at the interface
409 of each pair of neighboring cells. This segmented shape encompasses the cell-cell interface and any associated
410 protrusions from either neighboring cell. Last, to assign protrusions to the cell from which they originated, the
411 segmented region was divided in two by the shortest path between its bounding vertices that lay entirely within
412 the region. This approximates the position of the interface between the cells, and in subsequent steps we will
413 call this line “the interface”. Each of the two resulting protrusion shapes was assigned as originating from the cell
414 on the opposite side of the interface, because protrusions extend from one cell and overlap the other. Using this
415 approach, all of the protrusive structures that emerge from one cell, and that overlap a single neighboring cell, are
416 grouped together as a single segmented region for subsequent analysis.

417 **Measurement of membrane protrusivity, protrusion length, and protrusion orientation**

418 After segmenting cell edges and associated protrusions, we categorized them as either protrusive non-protrusive,
419 and then measured their lengths and orientations using Python scikit-fmm, scikit-image, and scipy libraries. We
420 use the term “membrane extensions” to refer to the cell edge shapes before the protrusive ones have been iden-
421 tified. To obtain a single measurement of length for each membrane extension, we first found its “tip”, defined
422 as the farthest pixel from any point along the interface. We then found its “base”, the point along the interface
423 that was closest to the tip. We defined membrane extension length as the length of the shortest path between
424 base and tip that lies entirely within the membrane extension. We defined membrane extension orientation as
425 the orientation of the vector from base to tip.

426 To categorize membrane extensions as protrusive or non-protrusive, we measured their length distribution in
427 CK-666-treated epithelia, which are nearly non-protrusive and so provided a measure of the width of the cell-cell
428 interface alone. For all conditions, we categorized a membrane extension as protrusive if its length was greater than

429 the 98th percentile of length of CK-666-treated epithelia. We then defined the protrusivity of an entire epithelium
430 as the ratio of protrusive to total cell edges in the field of view. Swarm plots of epithelial protrusivity and mean
431 membrane extension length were generated using GraphPad Prism 9 (GraphPad, San Diego, CA), as were all
432 other swarm plots. For analysis of protrusion orientation we included only the membrane extensions categorized
433 as protrusive. Polar histograms, generated in Python with matplotlib⁶³, show the distribution of protrusion
434 orientations. In these plots, bar area is proportional to the number of protrusions in the corresponding bin.

435 **Quantification of F-actin and Sra1-GFP cell-cell interface and non-interface basal surface fluo-** 436 **rescence**

437 Cells and cell-cell interfaces were segmented as described above. Cells and interfaces in contact with the tissue
438 border or image border were excluded from analysis. For interface fluorescence intensity, interfaces were dilated
439 by 5 pixels, and mean fluorescence intensity calculated from within this region. Non-interface basal surface fluo-
440 rescence intensity was calculated as the mean of the remaining (non-interface) tissue surface. For F-actin cell-cell
441 interface enrichment measurements, the overall brightness of the phalloidin staining varied between epithelia
442 independent of genotype. To control for this variation we subtracted the mean intensity of the epithelium's non-
443 interface basal surface from its mean interface intensity measurement. This value, the degree of F-actin interface
444 enrichment, was used as a proxy for F-actin protrusivity.

445 **Quantification of F-actin and Sra1-GFP planar polarity**

446 As a simple planar polarity measurement, we quantified mean F-actin (phalloidin) or Sra1-GFP fluorescence in-
447 tensity along each cell-cell interface as a function of the interface's orientation. To do this, cells and cell-cell in-
448 terfaces were segmented as described above. For interface angle measurements, the angular distance between the
449 line defined by the interface-bounding vertices and the anterior-posterior (horizontal) axis was calculated. For
450 interface fluorescence intensity measurements, interface regions were identified as segmented interfaces dilated
451 by 5 pixels. Vertices, dilated by 10 pixels, were excluded from interface regions. Mean fluorescence intensity was
452 calculated within each interface region, and background (the mean non-interface basal surface fluorescence in-
453 tensity of all cells in the image) was subtracted. To calculate the leading-trailing interface enrichment of F-actin
454 or Sra1-GFP for each egg chamber, interface fluorescence intensities were averaged for all interfaces with angles
455 between 0° and 10° (leading-trailing interfaces), and between 80° and 90° (side interfaces). The leading-trailing
456 interface enrichment is the ratio of these numbers.

457 **Autonomy analysis in mosaic epithelia**

458 Egg chambers were stained with Alexa FluorTM 647 phalloidin to mark protrusions, which indicate migration
459 direction, and to determine whether egg chambers were planar polarized. We analyzed only S6-7 egg chambers
460 with mixtures of control and *fat2* cells that had global stress fiber alignment orthogonal to the anterior-posterior
461 axis, indicating global planar polarity. Since migration is required to maintain planar polarity¹⁶, this also indicates
462 that the epithelium was migratory. Looking at phalloidin and genotype markers only, we drew 10 pixel-wide seg-
463 mented lines along leading-trailing interface boundaries of different genotype combinations in Fiji. Lines were
464 drawn along all visible, in-focus *fat2*-control and control-*fat2* boundaries and a similar number of control-control

465 and *fat2-fat2* boundaries. A boundary category was excluded if there were fewer than 3 usable interfaces to mea-
466 sure. Mean Sra1-GFP fluorescence intensities were calculated for each interface type in each egg chamber. For
467 a diagram of this method, see Barlan *et al.* (2017)¹⁴. To quantify non-interface basal surface fluorescence, we
468 drew polygonal regions of the basal surface of control and *fat2* cells, excluding cells immediately behind those of
469 a different genotype. Egg chambers were excluded if there were fewer than 3 usable cells of either genotype. Mean
470 Sra1-GFP fluorescence intensities were calculated within these polygonal regions for all control cells and all *fat2*
471 cells in an egg chamber.

472 **Quantification of migration rate**

473 Egg chambers were dissected, dyed with CellMask Orange, and mounted for live imaging as described above.
474 Several ovarioles were mounted on each slide, with each ovariole terminating in a S6-7 egg chamber. Timelapse
475 imaging was performed for 30 minutes with frames acquired every 30 seconds. Multi-point acquisition was used
476 to obtain movies of up to 5 egg chambers simultaneously. To generate a kymograph, a line was drawn along the
477 axis of migration at the center of the anterior-posterior egg chamber axis in Fiji. In these kymographs, cell-cell
478 interfaces are visible as lines, and their slope gives a measurement of cell migration rate. Egg chamber migration
479 rates were calculated from the average of 4 cell interface slopes from each kymograph. Egg chambers that clearly
480 slowed down over the course of the timelapse, visible as curvature in the interface lines in the kymographs, were
481 excluded. For an illustration of this method, see Barlan *et al.*¹⁴.

482 **Cell perimeter kymograph generation and interpretation**

483 To visualize the distribution of Sra1-GFP along cell-cell interfaces over time, we generated kymographs of cell
484 perimeters from timelapses of Sra1-GFP-expressing epithelia obtained using near-TIRF microscopy. Perimeters
485 were drawn manually in Fiji in each frame with the pencil tool, and then these perimeters were used to generate
486 kymographs in Python. Perimeters were thinned to 1 pixel and then perimeter pixels were sequenced with Python
487 scikit-image and scipy libraries. Kymographs were generated with matplotlib. Kymograph rows were constructed
488 by linearizing the perimeters from each frame, starting with the pixel directly above the cell centroid (the center of
489 the trailing edge in control cells) and continuing counter-clockwise. Each row shows the fluorescence intensity of
490 the perimeter pixels in sequence. Cell perimeter lengths varied between frames, so kymograph row lengths varied
491 and were aligned to their center position.

492 At the spatial and temporal resolution of the timelapses and corresponding kymographs, we cannot evaluate dif-
493 ferences in the dynamics the puncta-scale WAVE complex accumulations highlighted in Fig. 5. Instead, we focus
494 on the “region”-scale distribution of Sra1-GFP, and the stability of that distribution over time. The regions we
495 refer to here are approximately the length of a cell-cell interface, with variation. Because the kymographs are gen-
496 erated from epithelia in which all cells express Sra1-GFP, we need additional information to identify the cell to
497 which a region of Sra1-GFP enrichment belongs. We infer that Sra1-GFP is predominantly at leading edges in
498 polarized, migratory epithelia based on the Sra1-GFP distribution in epithelia with mosaic Sra1-GFP expression
499 (Fig. 3B). Based on consistent correlation between Sra1-GFP enrichment and the presence of protrusions (Fig.
500 3B, 4A, S7A), and its known role building lamellipodia as part of the WAVE complex^{17,18,39}, we also infer that

501 regions of Sra1-GFP enrichment belong to the cell that is protruding outward regardless of genotype. Our in-
502 terpretations of Sra1-GFP enrichment patterns in movies and corresponding kymographs are made with these
503 assumptions.

504 **Colocalization of proteins along the leading-trailing interface**

505 Data used for colocalization analysis were collected with 63x/1.4 NA Plan-APOCHROMAT oil immersion
506 objective to minimize chromatic aberration. Linescans were generated in Fiji by manually drawing a 10 pixel-
507 wide segmented line along rows of leading-trailing interfaces at the follicle cell basal surface. At least 20 leading-
508 trailing interfaces were included per egg chamber. Fluorescence intensities along the linescans were obtained
509 with the PlotProfile function, which averages pixel intensities along the width of the line and reports a list of
510 averaged values along the line's length. Spearman's correlation coefficients were calculated for each egg chamber
511 in Python with the scipy.stats module. Failure to exactly follow leading-trailing interfaces and cusps in the seg-
512 mented lines will artificially inflate the measured correlation, so we used correlation between E-cadherin-GFP⁶⁴
513 and Abi-mCherry as a negative control that would also be subject to this inflation. Abi-mCherry and E-cadherin-
514 GFP are slightly displaced from each other (anticorrelated) along the length of protrusions (the width of the
515 linescans), but averaging across the line width collapses this displacement, resulting in measured intensity signals
516 that are roughly uncorrelated. Spearman's correlation coefficients \pm standard deviation are reported in the text.
517 Linescans of leading-trailing interfaces were plotted using the fluorescence intensities from along the leading-
518 trailing interfaces of two cells. Intensities from each fluorophore were rescaled between 0 and 1 and plotted with
519 matplotlib in Python.

520 **Protrusion profile generation**

521 Viewing only the F-actin channel in Fiji, 1 pixel-wide lines were drawn down the length of F-actin bundles at the
522 leading edge. Fluorescence intensities along these lines were obtained for all fluorophores with the Fiji PlotProfile
523 function. In Python, these traces were aligned to the pixel with highest Fat2-3xGFP or Ena-GFP intensity (Fig.
524 5G, S8F). To calculate standard deviation, all traces were first rescaled individually so that their values ranged
525 between 0 and 1. To plot "protrusion profiles," the mean fluorescence was determined for each fluorophore at
526 each pixel position, and then average values were rescaled between 0 and 1. Plots of protrusion profiles were
527 generated with matplotlib.

528 **Movie generation**

529 Labels were added to timelapse movies in Fiji and then exported as .avi files. These were encoded as 1080p30
530 .mp4 files with H.264 (x264) video encoder using HandBrake 1.4.

531 **Reproducibility and statistical analysis**

532 Visibly damaged egg chambers were excluded from all analyses. Each experiment was performed at least two in-
533 dependent times, and results confirmed to be qualitatively consistent. Each experiment included egg chambers
534 pooled from multiple flies. Experiments and analysis were not randomized or performed blinded. Sample sizes

535 were not predetermined using a statistical method. The number of biological replicates (n), statistical tests per-
536 formed, and their significance can be found in figures or figure legends. Based on visual inspection, all data on
537 which statistical tests were performed followed an approximately normal distribution, so tests assuming normalcy
538 were used. Alpha was set to 0.05 for all statistical tests. Paired statistical tests were used for comparisons of cells
539 of different genetic conditions within mosaic epithelia, except if all epithelia did not have all genetic conditions
540 represented, in which case an unpaired test was used so that all samples could still be included. All t-tests were
541 two-tailed. One-sample t-tests were used when comparing a distribution of ratios to a null expectation of one. A
542 one-way ANOVA was used when multiple pairs of conditions were compared, with the exception of plots in Figs.
543 2C, S2A, and S3C, for which the variance did not appear consistent between conditions, so Welch’s ANOVA was
544 used instead. For post-hoc comparison tests, all pairs of conditions present in the corresponding plot were com-
545 pared using post-hoc Tukey’s multiple comparisons test with the following exception: the data plotted in Figs.
546 5E and S8B were analyzed together, and all conditions were compared to Fat2-Abi and E-cadherin-Abi only, and
547 in Fig. S6C only data from the same region (total, interface, or non-interface) was compared. For these, Šidák’s
548 multiple comparisons tests were used. For Welch’s ANOVA, Dunnett’s T3 multiple comparisons tests were used.
549 P-values reported for all post-hoc tests were adjusted for multiple comparisons. All statistical tests except for the
550 calculation of Spearman’s correlation coefficients were performed in GraphPad Prism 9.

551 References

- 552 1. Friedl, P. & Gilmour, D. Collective Cell Migration in Morphogenesis, Regeneration and Cancer. *Nature*
553 *Reviews Molecular Cell Biology* **10**, 445–457 (July 2009).
- 554 2. Scarpa, E. & Mayor, R. Collective Cell Migration in Development. *Journal of Cell Biology* **212**, 143–155
555 (Jan. 2016).
- 556 3. Norden, C. & Lecaudey, V. Collective Cell Migration: General Themes and New Paradigms. *Current Opin-*
557 *ion in Genetics & Development. Developmental Mechanisms, Patterning and Evolution* **57**, 54–60 (Aug.
558 2019).
- 559 4. Perez-Vale, K. Z. & Peifer, M. Orchestrating Morphogenesis: Building the Body Plan by Cell Shape Changes
560 and Movements. *Development* **147**, dev191049 (Sept. 2020).
- 561 5. Bodor, D. L., Pönisch, W., Endres, R. G. & Paluch, E. K. Of Cell Shapes and Motion: The Physical Basis
562 of Animal Cell Migration. *Developmental Cell* **52**, 550–562 (Mar. 2020).
- 563 6. Buttenschön, A. & Edelstein-Keshet, L. Bridging from Single to Collective Cell Migration: A Review of
564 Models and Links to Experiments. *PLOS Computational Biology* **16**, e1008411 (Dec. 2020).
- 565 7. Stock, J. & Pauli, A. Self-Organized Cell Migration across Scales – from Single Cell Movement to Tissue
566 Formation. *Development* **148** (Apr. 2021).
- 567 8. Duhart, J. C., Parsons, T. T. & Raftery, L. A. The Repertoire of Epithelial Morphogenesis on Display:
568 Progressive Elaboration of *Drosophila* Egg Structure. *Mechanisms of Development* **148**, 18–39 (Dec. 2017).
- 569 9. Gutzeit, H. O., Eberhardt, W. & Gratwohl, E. Laminin and Basement Membrane-Associated Microfila-
570 ments in Wild-Type and Mutant *Drosophila* Ovarian Follicles. *Journal of Cell Science* **100**, 781–788 (Dec.
571 1991).
- 572 10. Haigo, S. L. & Bilder, D. Global Tissue Revolutions in a Morphogenetic Movement Controlling Elonga-
573 tion. *Science* **331**, 1071–1074 (Feb. 2011).

- 574 11. Isabella, A. J. & Horne-Badovinac, S. Rab10-Mediated Secretion Synergizes with Tissue Movement to
575 Build a Polarized Basement Membrane Architecture for Organ Morphogenesis. *Developmental Cell* **38**,
576 47–60 (July 2016).
- 577 12. Crest, J., Diz-Muñoz, A., Chen, D.-Y., Fletcher, D. A. & Bilder, D. Organ Sculpting by Patterned Extracel-
578 lular Matrix Stiffness. *eLife* **6** (ed Spradling, A. C.) e24958 (June 2017).
- 579 13. Chen, D.-Y., Crest, J. & Bilder, D. A Cell Migration Tracking Tool Supports Coupling of Tissue Rotation
580 to Elongation. *Cell Reports* **21**, 559–569 (Oct. 2017).
- 581 14. Barlan, K., Cetera, M. & Horne-Badovinac, S. Fat2 and Lar Define a Basally Localized Planar Signaling
582 System Controlling Collective Cell Migration. *Developmental Cell* **40**, 467–477.e5 (Mar. 2017).
- 583 15. Stedden, C. G., Menegas, W., Zajac, A. L., Williams, A. M., Cheng, S., Özkan, E. & Horne-Badovinac,
584 S. Planar-Polarized Semaphorin-5c and Plexin A Promote the Collective Migration of Epithelial Cells in
585 *Drosophila*. *Current Biology* **29**, 908–920.e6 (Mar. 2019).
- 586 16. Cetera, M., Ramirez-San Juan, G. R., Oakes, P. W., Lewellyn, L., Fairchild, M. J., Tanentzapf, G., Gardel,
587 M. L. & Horne-Badovinac, S. Epithelial Rotation Promotes the Global Alignment of Contractile Actin
588 Bundles during *Drosophila* Egg Chamber Elongation. *Nature Communications* **5**, 5511 (Nov. 2014).
- 589 17. Miki, H., Suetsugu, S. & Takenawa, T. WAVE, a Novel WASP-family Protein Involved in Actin Reorgani-
590 zation Induced by Rac. *The EMBO Journal* **17**, 6932–6941 (Dec. 1998).
- 591 18. Miki, H., Yamaguchi, H., Suetsugu, S. & Takenawa, T. IRSp53 Is an Essential Intermediate between Rac
592 and WAVE in the Regulation of Membrane Ruffling. *Nature* **408**, 732–735 (Dec. 2000).
- 593 19. Chen, Z., Borek, D., Padrick, S. B., Gomez, T. S., Metlagel, Z., Ismail, A. M., Umetani, J., Billadeau, D. D.,
594 Otwinowski, Z. & Rosen, M. K. Structure and Control of the Actin Regulatory WAVE Complex. *Nature*
595 **468**, 533–538 (Nov. 2010).
- 596 20. Machesky, L. M., Mullins, R. D., Higgs, H. N., Kaiser, D. A., Blanchoin, L., May, R. C., Hall, M. E. & Pol-
597 lard, T. D. Scar, a WASP-related Protein, Activates Nucleation of Actin Filaments by the Arp2/3 Complex.
598 *Proceedings of the National Academy of Sciences* **96**, 3739–3744 (Mar. 1999).
- 599 21. Bieling, P., Hansen, S. D., Akin, O., Li, T.-D., Hayden, C. C., Fletcher, D. A. & R Dyche, M. WH2 and
600 Proline-Rich Domains of WASP-family Proteins Collaborate to Accelerate Actin Filament Elongation. *The*
601 *EMBO Journal* **37**, 102–121 (Jan. 2018).
- 602 22. Mullins, R. D., Bieling, P. & Fletcher, D. A. From Solution to Surface to Filament: Actin Flux into Branched
603 Networks. *Biophysical Reviews* **10**, 1537–1551 (Dec. 2018).
- 604 23. Viktorinová, I., König, T., Schlichting, K. & Dahmann, C. The Cadherin Fat2 Is Required for Planar Cell
605 Polarity in the *Drosophila* Ovary. *Development* **136**, 4123–4132 (Dec. 2009).
- 606 24. Viktorinová, I. & Dahmann, C. Microtubule Polarity Predicts Direction of Egg Chamber Rotation in
607 *Drosophila*. *Current Biology* **23**, 1472–1477 (Aug. 2013).
- 608 25. Squarr, A. J., Brinkmann, K., Chen, B., Steinbacher, T., Ebnet, K., Rosen, M. K. & Bogdan, S. Fat2 Acts
609 through the WAVE Regulatory Complex to Drive Collective Cell Migration during Tissue Rotation. *Jour-
610 nal of Cell Biology* **212**, 591–603 (Feb. 2016).
- 611 26. Weiner, O. D., Marganski, W. A., Wu, L. F., Altschuler, S. J. & Kirschner, M. W. An Actin-Based Wave
612 Generator Organizes Cell Motility. *PLOS Biology* **5**, e221 (Aug. 2007).
- 613 27. Iglesias, P. A. & Devreotes, P. N. Biased Excitable Networks: How Cells Direct Motion in Response to
614 Gradients. *Current Opinion in Cell Biology. Cell Regulation* **24**, 245–253 (Apr. 2012).
- 615 28. Aurich, F. & Dahmann, C. A Mutation in Fat2 Uncouples Tissue Elongation from Global Tissue Rotation.
616 *Cell Reports* **14**, 2503–2510 (Mar. 2016).
- 617 29. Chen, X. J., Squarr, A. J., Stephan, R., Chen, B., Higgins, T. E., Barry, D. J., Martin, M. C., Rosen, M. K.,
618 Bogdan, S. & Way, M. Ena/VASP Proteins Cooperate with the WAVE Complex to Regulate the Actin
619 Cytoskeleton. *Developmental Cell* **30**, 569–584 (Sept. 2014).

- 620 30. Krueger, N. X., Vactor, D. V., Wan, H. I., Gelbart, W. M., Goodman, C. S. & Saito, H. The Transmembrane Tyrosine Phosphatase DLAR Controls Motor Axon Guidance in *Drosophila*. *Cell* **84**, 611–622 (Feb. 1996).
- 621
622
- 623 31. Frydman, H. M. & Spradling, A. C. The Receptor-like Tyrosine Phosphatase Lar Is Required for Epithelial Planar Polarity and for Axis Determination with *Drosophila* Ovarian Follicles. *Development* **128**, 3209–3220 (Aug. 2001).
- 624
625
- 626 32. Das, T., Safferling, K., Rausch, S., Grabe, N., Boehm, H. & Spatz, J. P. A Molecular Mechanotransduction Pathway Regulates Collective Migration of Epithelial Cells. *Nature Cell Biology* **17**, 276–287 (Mar. 2015).
- 627
- 628 33. Jain, S., Cachoux, V. M. L., Narayana, G. H. N. S., de Beco, S., D’Alessandro, J., Cellerin, V., Chen, T., Heuzé, M. L., Marcq, P., Mège, R.-M., Kabla, A. J., Lim, C. T. & Ladoux, B. The Role of Single-Cell Mechanical Behaviour and Polarity in Driving Collective Cell Migration. *Nature Physics* **16**, 802–809 (July 2020).
- 629
630
631
- 632 34. Hayer, A., Shao, L., Chung, M., Joubert, L.-M., Yang, H. W., Tsai, F.-C., Bisaria, A., Betzig, E. & Meyer, T. Engulfed Cadherin Fingers Are Polarized Junctional Structures between Collectively Migrating Endothelial Cells. *Nature Cell Biology* **18**, 1311–1323 (Dec. 2016).
- 633
634
- 635 35. Xiong, Y., Huang, C.-H., Iglesias, P. A. & Devreotes, P. N. Cells Navigate with a Local-Excitation, Global-Inhibition-Biased Excitable Network. *Proceedings of the National Academy of Sciences* **107**, 17079–17086 (Oct. 2010).
- 636
637
- 638 36. Graziano, B. R. & Weiner, O. D. Self-Organization of Protrusions and Polarity during Eukaryotic Chemotaxis. *Current Opinion in Cell Biology* **30**, 60–67 (Oct. 2014).
- 639
- 640 37. Oikawa, T., Yamaguchi, H., Itoh, T., Kato, M., Ijuin, T., Yamazaki, D., Suetsugu, S. & Takenawa, T. PtdIns(3,4,5)P₃ Binding Is Necessary for WAVE2-induced Formation of Lamellipodia. *Nature Cell Biology* **6**, 420–426 (May 2004).
- 641
642
- 643 38. Lebensohn, A. M. & Kirschner, M. W. Activation of the WAVE Complex by Coincident Signals Controls Actin Assembly. *Molecular Cell* **36**, 512–524 (Nov. 2009).
- 644
- 645 39. Steffen, A., Rottner, K., Ehinger, J., Innocenti, M., Scita, G., Jürgen, W. & Stradal, T. E. Sra-1 and Nap1 Link Rac to Actin Assembly Driving Lamellipodia Formation. *The EMBO Journal* **23**, 749–759 (Feb. 2004).
- 646
647
- 648 40. Sossey-Alaoui, K., Li, X., Ranalli, T. A. & Cowell, J. K. WAVE3-mediated Cell Migration and Lamellipodia Formation Are Regulated Downstream of Phosphatidylinositol 3-Kinase*. *Journal of Biological Chemistry* **280**, 21748–21755 (June 2005).
- 649
650
- 651 41. Weiner, O. D., Rentel, M. C., Ott, A., Brown, G. E., Jedrychowski, M., Yaffe, M. B., Gygi, S. P., Cantley, L. C., Bourne, H. R. & Kirschner, M. W. Hem-1 Complexes Are Essential for Rac Activation, Actin Polymerization, and Myosin Regulation during Neutrophil Chemotaxis. *PLOS Biology* **4**, e38 (Jan. 2006).
- 652
653
- 654 42. Nakao, S., Platek, A., Hirano, S. & Takeichi, M. Contact-Dependent Promotion of Cell Migration by the OL-protocadherin–Nap1 Interaction. *Journal of Cell Biology* **182**, 395–410 (July 2008).
- 655
- 656 43. Chen, B., Brinkmann, K., Chen, Z., Pak, C. W., Liao, Y., Shi, S., Henry, L., Grishin, N. V., Bogdan, S. & Rosen, M. K. The WAVE Regulatory Complex Links Diverse Receptors to the Actin Cytoskeleton. *Cell* **156**, 195–207 (Jan. 2014).
- 657
658
- 659 44. Truong Quang, B.-A., Mani, M., Markova, O., Lecuit, T. & Lenne, P.-F. Principles of E-Cadherin Supramolecular Organization In Vivo. *Current Biology* **23**, 2197–2207 (Nov. 2013).
- 660
- 661 45. Rubinstein, R., Goodman, K. M., Maniatis, T., Shapiro, L. & Honig, B. Structural Origins of Clustered Protocadherin-Mediated Neuronal Barcoding. *Seminars in Cell & Developmental Biology. Spectraplakins, Versatile Roles in Physiology and Pathology* **69**, 140–150 (Sept. 2017).
- 662
663
- 664 46. Li, J. X. H., Tang, V. W., Boateng, K. A. & Briehner, W. M. Cadherin Puncta Are Interdigitated Dynamic Actin Protrusions Necessary for Stable Cadherin Adhesion. *Proceedings of the National Academy of Sciences* **118** (June 2021).
- 665
666

- 667 47. Strutt, H., Warrington, S. J. & Strutt, D. Dynamics of Core Planar Polarity Protein Turnover and Stable
668 Assembly into Discrete Membrane Subdomains. *Developmental Cell* **20**, 511–525 (Apr. 2011).
- 669 48. Cho, B., Pierre-Louis, G., Sagner, A., Eaton, S. & Axelrod, J. D. Clustering and Negative Feedback by En-
670 docytosis in Planar Cell Polarity Signaling Is Modulated by Ubiquitinylation of Prickle. *PLoS Genetics* **11**,
671 e1005259 (May 2015).
- 672 49. Stahley, S. N., Basta, L. P., Sharan, R. & Devenport, D. Celsr1 Adhesive Interactions Mediate the Asym-
673 metric Organization of Planar Polarity Complexes. *eLife* **10** (eds Weis, W. I. & Akhmanova, A.) e62097
674 (Feb. 2021).
- 675 50. Hayashi, S., Ito, K., Sado, Y., Taniguchi, M., Akimoto, A., Takeuchi, H., Aigaki, T., Matsuzaki, F., Nak-
676 agoshi, H., Tanimura, T., Ueda, R., Uemura, T., Yoshihara, M. & Goto, S. GETDB, a Database Compiling
677 Expression Patterns and Molecular Locations of a Collection of Gal4 Enhancer Traps. *genesis* **34**, 58–61
678 (2002).
- 679 51. Golic, K. G. & Lindquist, S. The FLP Recombinase of Yeast Catalyzes Site-Specific Recombination in the
680 *Drosophila* Genome. *Cell* **59**, 499–509 (Nov. 1989).
- 681 52. Golic, K. G. Site-Specific Recombination Between Homologous Chromosomes in *Drosophila*. *Science* **252**,
682 958–961 (May 1991).
- 683 53. Gratz, S. J., Cummings, A. M., Nguyen, J. N., Hamm, D. C., Donohue, L. K., Harrison, M. M., Wildonger,
684 J. & O’Connor-Giles, K. M. Genome Engineering of *Drosophila* with the CRISPR RNA-Guided Cas9
685 Nuclease. *Genetics* **194**, 1029–1035 (Aug. 2013).
- 686 54. Gratz, S. J., Ukken, F. P., Rubinstein, C. D., Thiede, G., Donohue, L. K., Cummings, A. M. & O’Connor-
687 Giles, K. M. Highly Specific and Efficient CRISPR/Cas9-Catalyzed Homology-Directed Repair in *Drosophila*.
688 *Genetics* **196**, 961–971 (Apr. 2014).
- 689 55. Port, F., Chen, H.-M., Lee, T. & Bullock, S. L. Optimized CRISPR/Cas Tools for Efficient Germline and
690 Somatic Genome Engineering in *Drosophila*. *Proceedings of the National Academy of Sciences* **111**, E2967–
691 E2976 (July 2014).
- 692 56. Cetera, M., Lewellyn, L. & Horne-Badovinac, S. in *Drosophila: Methods and Protocols* (ed Dahmann, C.)
693 215–226 (Springer, New York, NY, 2016).
- 694 57. Spracklen, A. J., Fagan, T. N., Lovander, K. E. & Tootle, T. L. The Pros and Cons of Common Actin
695 Labeling Tools for Visualizing Actin Dynamics during *Drosophila* Oogenesis. *Developmental Biology* **393**,
696 209–226 (Sept. 2014).
- 697 58. Schindelin, J., Arganda-Carreras, I., Frise, E., Kaynig, V., Longair, M., Pietzsch, T., Preibisch, S., Rueden,
698 C., Saalfeld, S., Schmid, B., Tinevez, J.-Y., White, D. J., Hartenstein, V., Eliceiri, K., Tomancak, P. & Car-
699 dona, A. Fiji: An Open-Source Platform for Biological-Image Analysis. *Nature Methods* **9**, 676–682 (July
700 2012).
- 701 59. Schindelin, J., Rueden, C. T., Hiner, M. C. & Eliceiri, K. W. The ImageJ Ecosystem: An Open Platform
702 for Biomedical Image Analysis. *Molecular Reproduction and Development* **82**, 518–529 (2015).
- 703 60. Van der Walt, S., Schönberger, J. L., Nunez-Iglesias, J., Boulogne, F., Warner, J. D., Yager, N., Gouillart, E.
704 & Yu, T. Scikit-Image: Image Processing in Python. *PeerJ* **2**, e453 (June 2014).
- 705 61. Virtanen, P. *et al.* SciPy 1.0: Fundamental Algorithms for Scientific Computing in Python. *Nature Methods*
706 **17**, 261–272 (Mar. 2020).
- 707 62. napari contributors. *Napari: A Multi-Dimensional Image Viewer for Python* 2019.
- 708 63. Hunter, J. D. Matplotlib: A 2D Graphics Environment. *Computing in Science & Engineering* **9**, 90–95
709 (May 2007).
- 710 64. Huang, J., Zhou, W., Dong, W., Watson, A. M. & Hong, Y. Directed, Efficient, and Versatile Modifications
711 of the *Drosophila* Genome by Genomic Engineering. *Proceedings of the National Academy of Sciences* **106**,
712 8284–8289 (May 2009).

713 **Supplemental Figures**

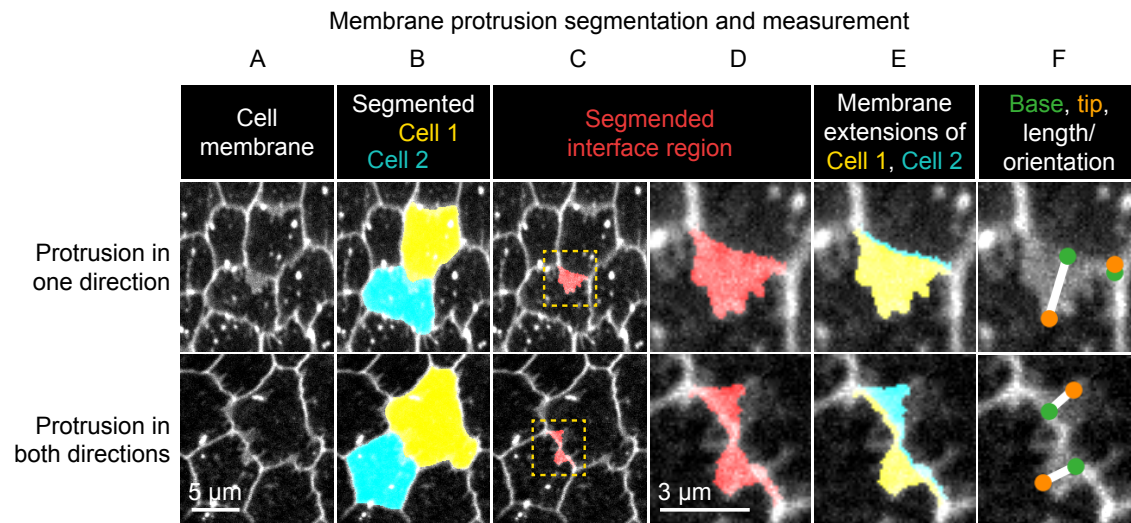


Figure S1: **Method used to segment and measure membrane protrusions.** Top row shows an example of a pair of neighboring cells in which one cell is protruding across their shared interface. Bottom row shows a case in which both cells are protruding across the interface. **A**, Cell interfaces and protrusions were labeled with a membrane dye and timelapses of the basal surface were collected. **B**, Cells were automatically segmented with a watershed-based method, and segmentation errors were hand-corrected. **C**, The bright interface region between each pair of neighboring cells was identified using a watershed-based method. This region includes the interface and any membrane protrusions that extend across it. **D**, An enlargement of the boxed regions of (C). **E**, The interface region was divided into two parts by the shortest path from vertex to vertex within the region, which approximates the true cell-cell interface position. The two resulting regions were then assigned to the cell they extend from. **F**, The tip and base of each region were identified, and the line from base to tip used to define their length and orientation. Associated with Fig. 2.

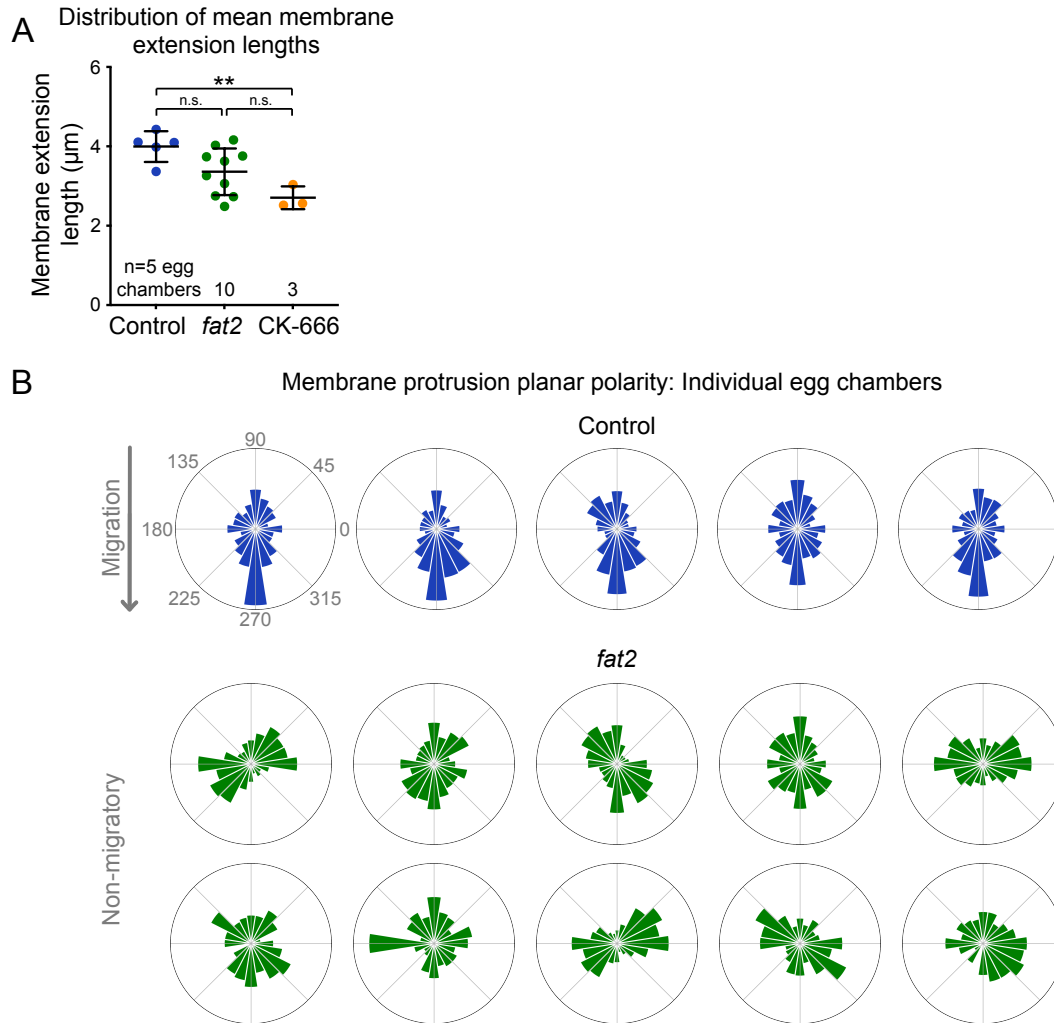


Figure S2: Membrane extension length and protrusion orientation in individual egg chambers **A**, Plot showing mean membrane extension lengths in control, *fat2*, and CK-666-treated egg chambers. Their length in *fat2* egg chambers is intermediate between control and CK-666, with a wider distribution that overlaps both. Welch's ANOVA ($W(2,7.31)=13.3$, $p=0.0037$) with Dunnett's T3 multiple comparisons test; n.s. (left to right) $p=0.077$, 0.081 , $**p=0.008$. **B**, Polar histograms showing the distribution of membrane protrusion orientations in individual control and *fat2* egg chambers. Anterior is left, posterior is right, and images were flipped as needed so that migration is downward for control epithelia, in which membrane protrusions are biased in the direction of migration. In *fat2* epithelia, protrusions have varying levels of axial bias and little or no vectorial bias. Associated with Fig. 2.

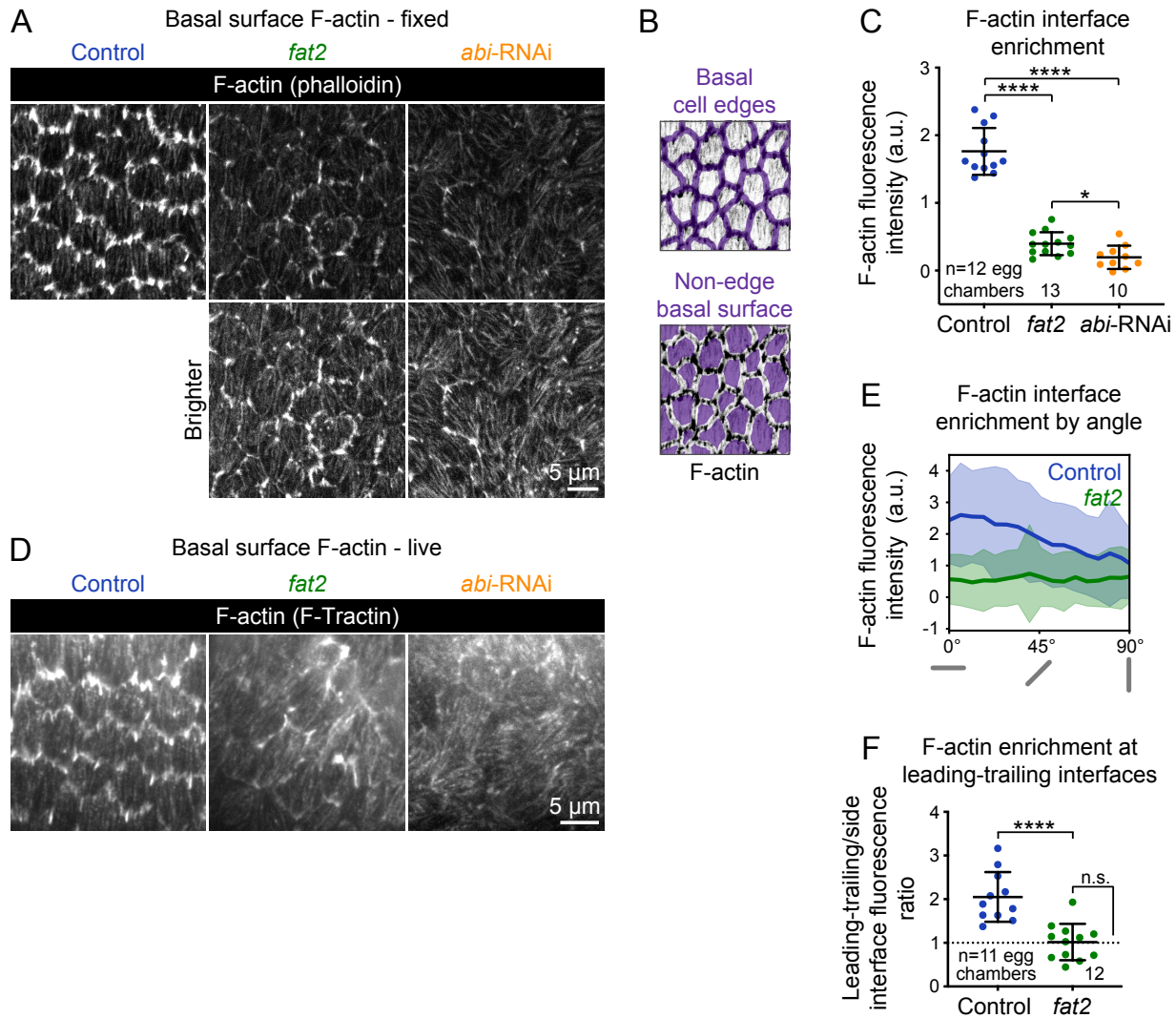


Figure S3: Actin protrusions are reduced and unpolarized without Fat2 and further reduced without the WAVE complex. **A**, Images showing phalloidin staining of F-actin in control, *fat2*, and *abi-RNAi*-expressing epithelia. Bottom row shows the same images with brighter display settings. From dataset quantified in C,E,F. **B**, Examples of segmented cell-cell interfaces or non-interface basal surfaces overlaid on F-actin. **C**, Plot of the difference in F-actin fluorescence intensity between cell interfaces and non-interface basal surfaces shows that while *fat2* and *abi-RNAi* epithelia have less F-actin interface enrichment than control epithelia, F-actin interface enrichment remains higher in *fat2* epithelia than *abi-RNAi* epithelia. Welch's ANOVA ($W(2, 19.84)=94.68, p<0.0001$) with Dunnett's T3 multiple comparisons test; * $p=0.033$, **** $p<0.0001$. **D**, Frames from timelapse images of control, *fat2*, and *abi-RNAi* epithelia with F-actin labeled with F-Tractin-tdTomato. As with phalloidin staining, the protrusivity of *fat2* epithelia is intermediate between that of control and *abi-RNAi* epithelia. Brightness display settings vary between genotypes to correct for variability in F-Tractin-tdTomato expression levels. See related Movie 3. **E**, Plot of F-actin fluorescence intensity at cell interfaces as a function of interface angular distance from horizontal. Gray bars below the X axis represent interface angles. **F**, Plot of the F-actin fluorescence ratio between leading-trailing (0-10°) and side (80-90°) interfaces, a measure of F-actin enrichment along leading-trailing interfaces. Egg chambers at $y=1$ (dashed line) have no enrichment. F-actin is enriched at leading-trailing interfaces in control, but not *fat2*, egg chambers. Control-*fat2* comparisons: unpaired t-test, **** $p<0.0001$. *fat2*-1 comparisons: one sample t-test, n.s. $p=0.88$. **C,E,F**, Bars (C,F) or lines and shaded regions (E) indicate mean \pm SD. Associated with Fig. 2; Movie 3.

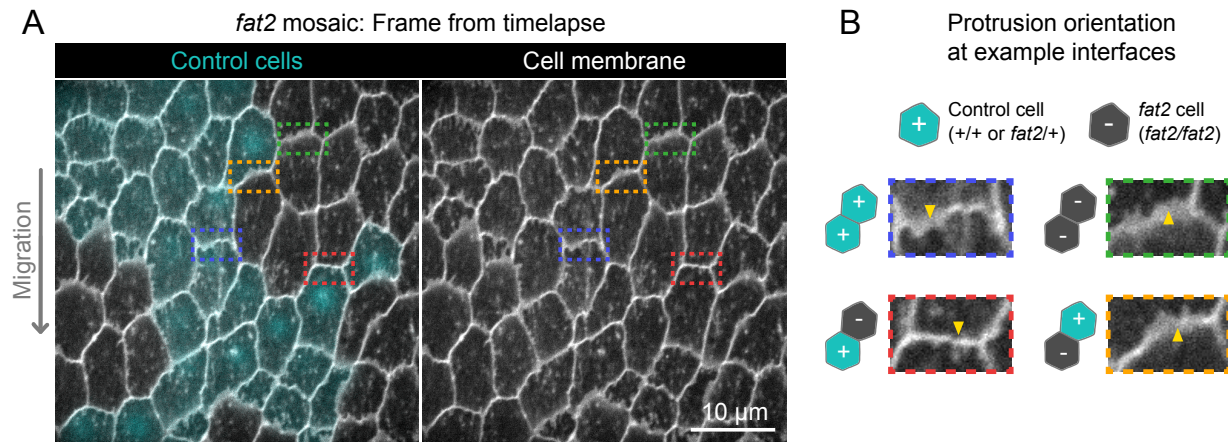


Figure S4: **Fat2 acts locally across the cell interface to orient membrane protrusions.** **A**, Timelapse frame of a *fat2* mosaic epithelium with cell membrane labeled, used to evaluate protrusion orientations in control or *fat2* cells within a migratory context. Boxes indicate examples of leading-trailing interfaces between neighbor pairs with each possible combination of genotypes. See related Movie 4. **B**, Larger images of the interfaces boxed in (A), showing that protrusions are misoriented when *fat2* cells are ahead of the interface regardless of the genotype of the cell behind the interface. Arrows point in the direction of protrusion. Associated with Fig. 2; Movie 4.

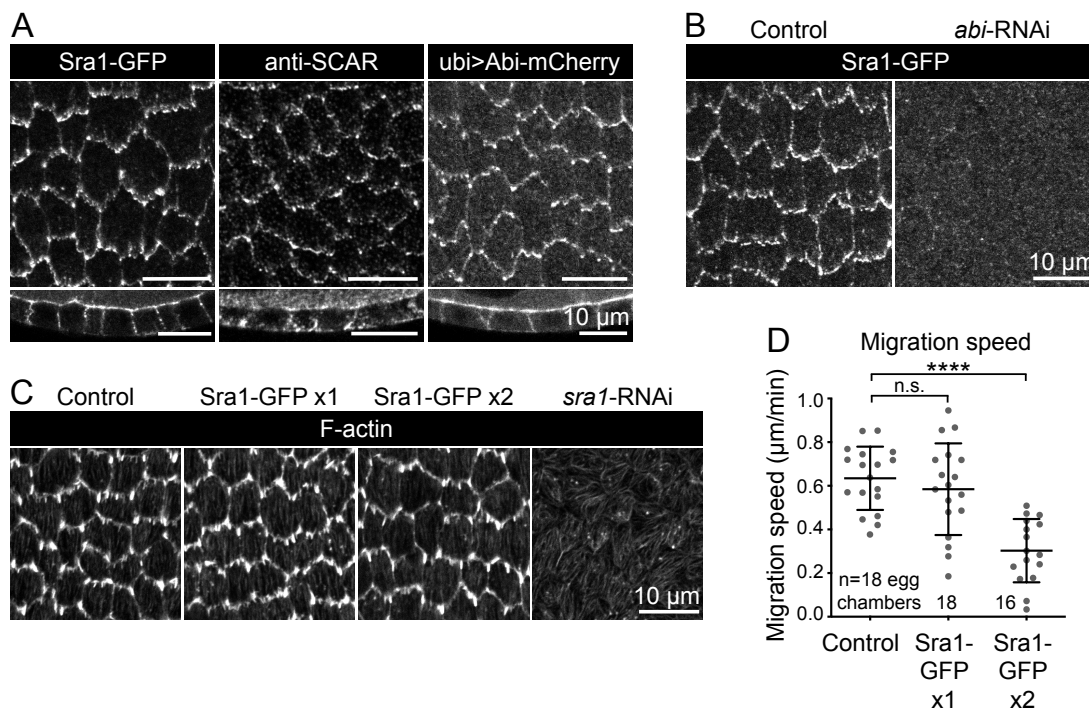


Figure S5: **Evaluation of endogenous Sra1-GFP functionality.** **A**, Images comparing the localization of markers of WAVE complex subunits: Sra1-GFP, Scar antibody, and Abi-mCherry, at the basal surface (top row) and in cross-section (bottom row). **B**, Images of Sra1-GFP localization in control and *abi*-RNAi-expressing epithelia. Sra1-GFP is dispersed in the absence of Abi. **C**, Images showing phalloidin-stained F-actin in epithelia with wild-type Sra1, one or two copies of Sra1-GFP, or expressing *sra1*-RNAi, used to assess the appearance of protrusions in each condition. **D**, Plot of migration speed of epithelia with wild-type Sra1 or one or two copies of Sra1-GFP. Migration speed is reduced when both Sra1 copies are GFP-tagged. One-way ANOVA ($F(2,49)=18.37$, $p<0.0001$) with post-hoc Tukey's test; n.s. 0.66, **** $p<0.0001$. See related Movie 5. Associated with Fig. 3; Movie 5.

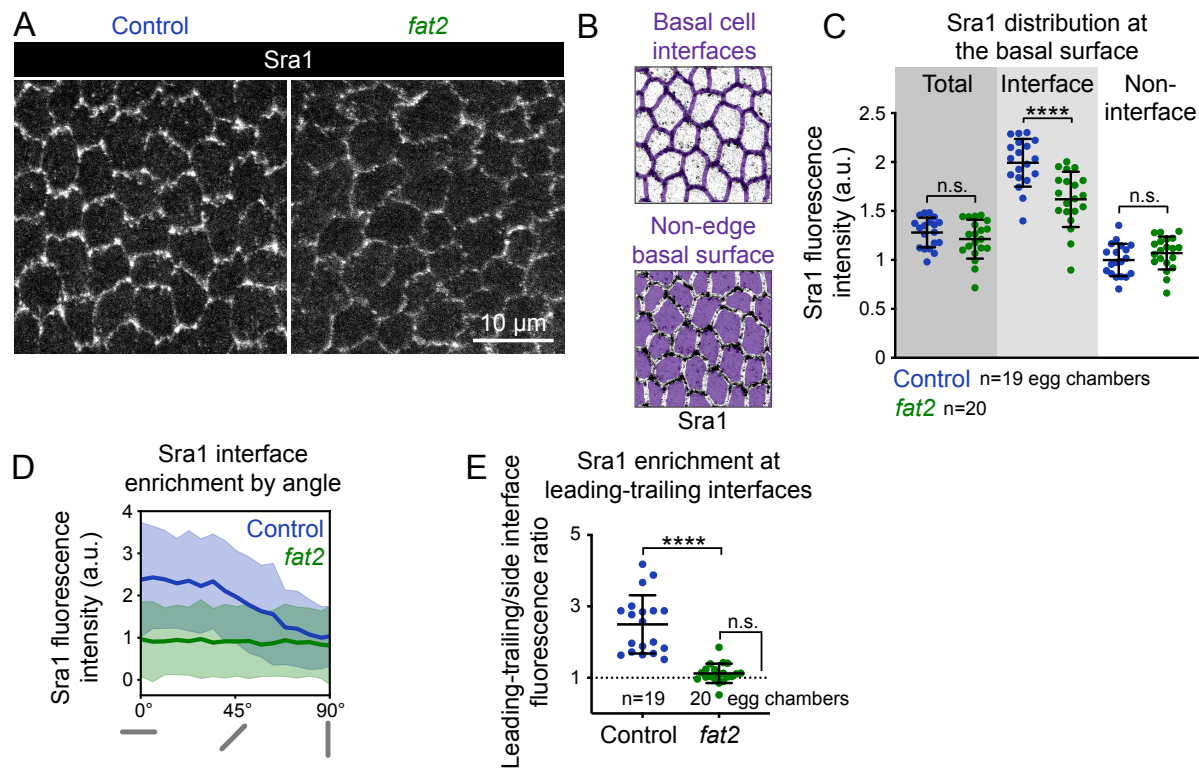


Figure S6: **Fat2 concentrates the WAVE complex at cell-cell interfaces and polarizes it across the epithelium.** **A**, Images of Sra1-GFP at the basal surface in control and *fat2* epithelia. **B**, Examples of segmented cell-cell interfaces or non-interface basal surfaces overlaid on Sra1-GFP images. **C**, Plot of mean Sra1-GFP fluorescence intensity across the entire basal surface (total), at cell-cell interfaces, and at non-interface basal surfaces in control and *fat2* epithelia. One-way ANOVA ($F(5,111)=63.22$, $p<0.0001$) with post-hoc Šidák's test; n.s. (left to right) $p=0.67$, 0.64 , $****p<0.0001$. **D**, Plot of Sra1-GFP fluorescence at cell-cell interfaces as a function of interface angular distance from horizontal. Gray bars below the X axis represent interface angles. **E**, Plot of the Sra1-GFP fluorescence intensity ratio between leading-trailing ($0-10^\circ$) and side ($80-90^\circ$) interfaces, a measure of Sra1-GFP enrichment along leading-trailing interfaces. Egg chambers at $y=1$ (dashed line) have no enrichment. Sra1-GFP is enriched at leading-trailing interfaces in control, but not *fat2*, epithelia. Control-*fat2* comparison: unpaired t-test, $****p<0.0001$. *fat2-1* comparison: one sample t-test, n.s. $p=0.052$. Bars (C,E) or lines and shaded regions (D) indicate mean \pm SD. Associated with Fig. 3.

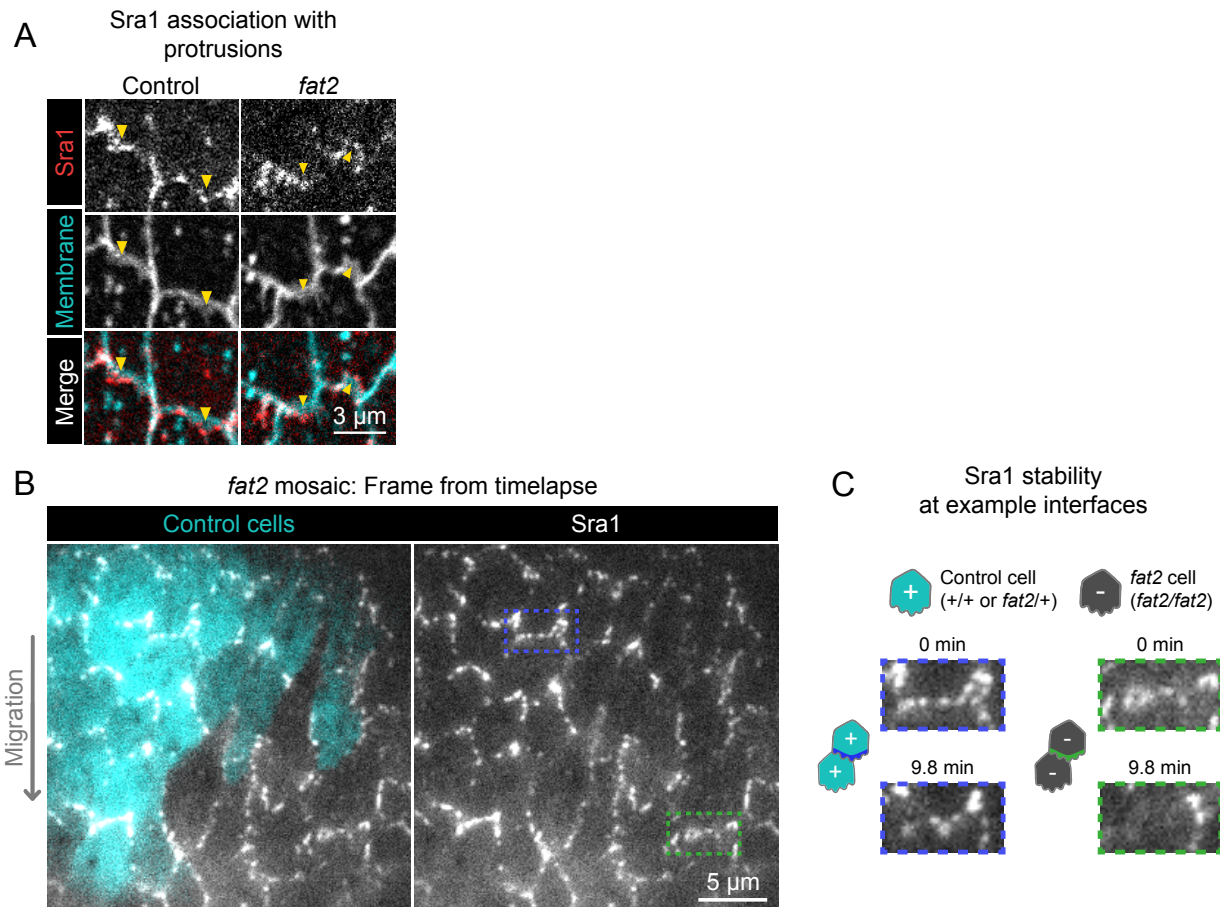


Figure S7: **Fat2 stabilizes domains of WAVE complex enrichment locally across the cell-cell interface.** **A**, Timelapse frames showing pairs of cell interfaces from control or *fat2* epithelia expressing Sra1-GFP and labeled with a membrane dye. Arrows indicate membrane protrusions. Sra1-GFP is enriched at protrusion tips in both control and *fat2* epithelia. See related Movie 6. **B**, Timelapse frame of a *fat2* mosaic epithelium in which all cells express Sra1-GFP, used to evaluate Sra1-GFP dynamics in control or *fat2* cells within a migratory context. Boxes indicate a leading-trailing interface between two control cells (blue) or *fat2* cells (green). See related Movie 10. **C**, Larger images of the interfaces boxed in (B), taken 9.8 minutes apart. Sra1-GFP is initially enriched along both interfaces. It remains enriched in the control interface throughout, but loses enrichment along the *fat2* interface. Associated with Fig. 4; Movies 6, 10.

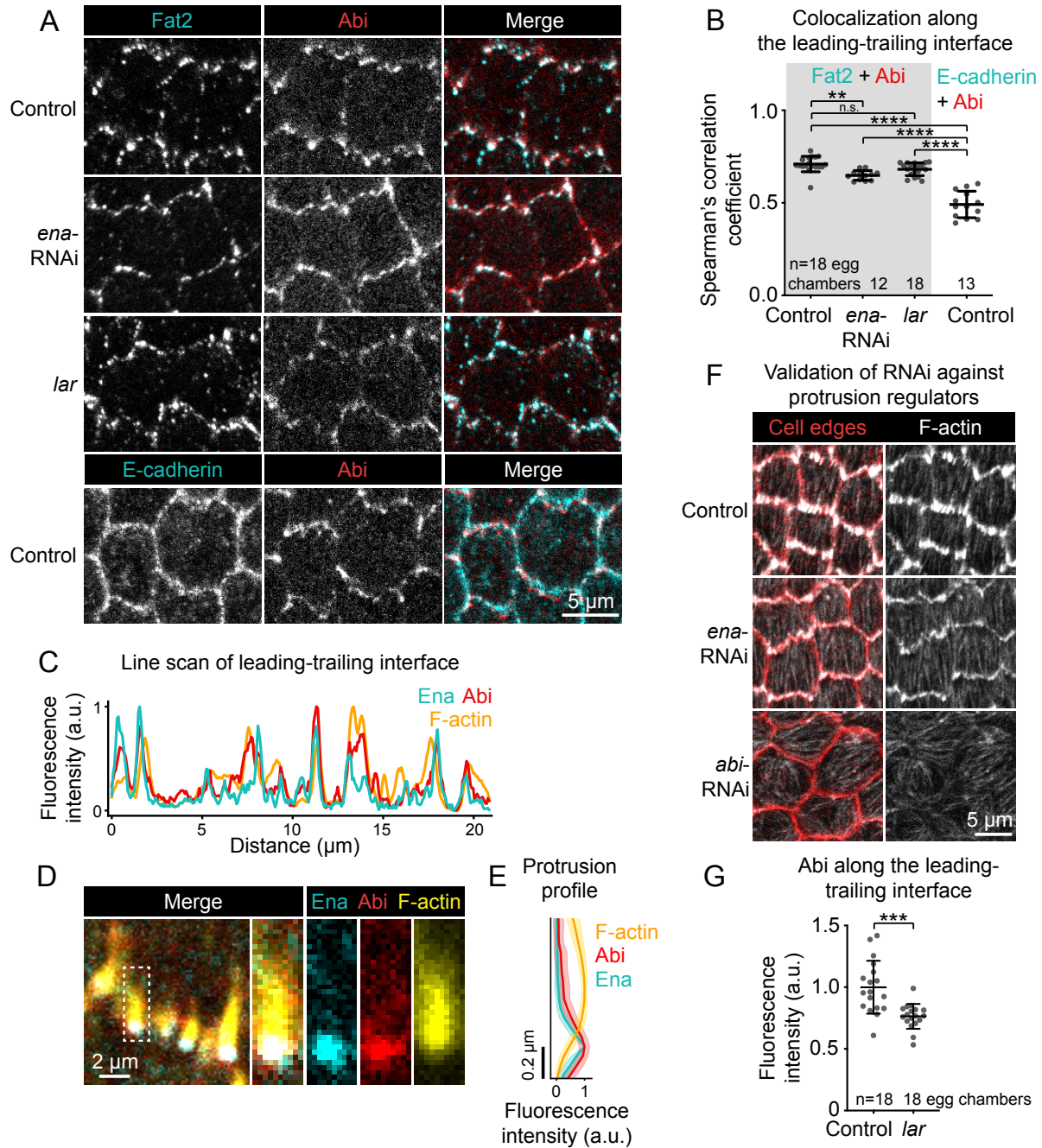


Figure S8: *Ena* and *Lar* are not required for colocalization between *Fat2* and the *WAVE* complex. **A**, Images of cells expressing *Fat2*-3xGFP and *Abi*-mCherry in control, *lar*, and *ena*-RNAi backgrounds (top 3 rows) or *E-cadherin*-GFP and *Abi*-mCherry (bottom row, negative control for colocalization measurements). **B**, Plot of Spearman's correlation coefficients of *Abi*-mCherry and *Fat2*-3xGFP (gray background) or *E-cadherin*-GFP (white background) show that *Fat2* and *Abi* colocalize in all three conditions more strongly than *E-cadherin* and *Abi*. Bars indicate mean \pm SD. One-way ANOVA ($F(4,69)=52.96$, $p<0.0001$) with post-hoc Tukey's test; n.s. $p=0.41$, ** $p<0.0046$, **** $p<0.0001$. **A,B**, Control *Fat2*-3xGFP and *Abi*-mCherry images and Spearman's coefficients are also in Fig. 5A,E. **C**, Line scan of GFP-*Ena*, *Abi*-mCherry, and F-actin (phalloidin) fluorescence intensity along a leading-trailing interface region, showing their corresponding peaks of enrichment. **D**, Image showing the GFP-*Ena*, *Abi*-mCherry, and F-actin (phalloidin) at the leading edge and in the boxed filopodium. **E**, Plot of mean fluorescence intensity of F-actin, *Abi*-mCherry, and GFP-*Ena* along the length of filopodia showing their relative distribution. Lines and shaded regions indicate mean \pm SD. $n=54$ filopodia (used for SD), 39 cells from 2 egg chambers. **F**, Images of F-actin (phalloidin) and cell interfaces (anti-Discs Large) in control, *ena*-RNAi, and *abi*-RNAi backgrounds. Expression of *ena*-RNAi strongly depletes filopodia, and *abi*-RNAi expression removes both filopodia and lamellipodia. **G**, Plot of mean fluorescence intensity of *Abi*-mCherry along leading-trailing interfaces in control epithelia or similarly-oriented interfaces in *lar* epithelia, some of which are non-migratory. Associated with Fig. 5.

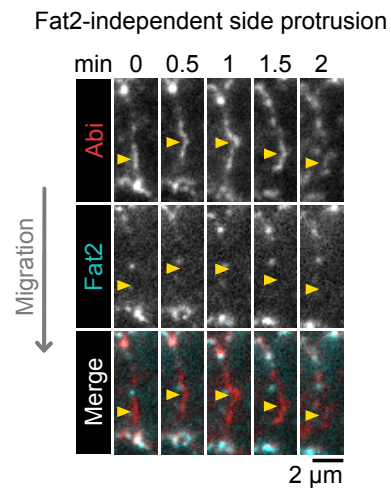


Figure S9: **The WAVE complex occasionally accumulates at side-facing interfaces away from Fat2.** Timelapse frames of a side-facing cell-cell interface from an epithelium expressing Abi-mCherry and Fat2-3xGFP. Arrows indicate a site of transient Abi-mCherry accumulation, protrusion, and dissipation with no corresponding Fat2-3xGFP enrichment. See related Movie 12. Associated with Fig. 5; Movie 12.

714 **Movie captions**

Movie 1: **Membrane protrusivity of control, *fat2*, and CK-666-treated epithelia.** Control, *fat2*, and CK-666-treated epithelia labeled with a membrane dye. Bottom row shows segmented edges. Protrusive edges, defined as ones with membrane extensions longer than the 98th percentile of those of CK-666-treated epithelia, are red. Non-protrusive edges are white. Acquired with laser scanning confocal microscope. Associated with Fig. 2A.

Movie 2: **Protrusion orientation in control and *fat2* epithelia.** Control and *fat2* epithelia are labeled with a membrane dye, and arrows indicating the orientation of protrusions are overlaid. Arrows originate at protrusion bases and have lengths proportional to protrusion lengths. Acquired with laser scanning confocal microscope. Associated with Fig. 2A.

Movie 3: **F-actin protrusivity and protrusion polarity of control and *fat2* epithelia.** Control, *fat2*, and *abi*-RNAi epithelia with F-actin labeled with F-Tractin-tdTomato. The protrusivity of *fat2* epithelia is intermediate between that of control and *abi*-RNAi epithelia. Brightness display settings vary between genotypes to correct for variability in F-Tractin-tdTomato expression levels. Acquired with TIRF microscope. Associated with Fig. S3D.

Movie 4: **Membrane protrusion in a *fat2* mosaic epithelium.** A *fat2* mosaic epithelium with cell membrane labeled, used to evaluate protrusion orientations in control or *fat2* cells within a migratory context. Boxes indicate examples of leading-trailing interfaces between neighbor pairs with each possible combination of genotypes. Acquired with laser scanning confocal microscope. Associated with Fig. S4.

Movie 5: **Migration of epithelia with endogenously-tagged Sra1-GFP.** Epithelia with unlabeled Sra1 (Control), one copy of Sra1-GFP and one unlabeled Sra1, or two copies of Sra1-GFP, imaged at the mid-plane between apical and basal cell surfaces. Representative of timelapses used to measure migration speed. Acquired with laser scanning confocal microscope. Associated with Fig. S5D.

Movie 6: **Sra1 enrichment at protrusion tips in control and *fat2* epithelia.** Pairs of cell edges from control or *fat2* epithelia expressing Sra1-GFP and labeled with a membrane dye. Sra1-GFP is enriched at protrusion tips in both control and *fat2* epithelia. Associated with Fig. S7A.

Movie 7: **WAVE complex-enriched domain dynamics in control and *fat2* cells.** Cells from control and *fat2* epithelia expressing Sra1-GFP. Laser intensity and brightness display settings differ between genotypes. Used to evaluate the stability of domains of Sra1-GFP accumulation. Associated with Fig. 4B,D.

Movie 8: **WAVE complex-enriched domain dynamics in control and *fat2* epithelia.** Fields of cells from control and *fat2* epithelia expressing Sra1-GFP. Laser intensity and brightness display settings differ between genotypes. Used to evaluate the stability of domains of Sra1-GFP accumulation. Wider view of the epithelia shown in Fig. 4B,D.

Movie 9: **Dynamics of protrusive domains in control and *fat2* cells.** Top row shows the interfaces and membrane protrusions of one cell and its neighbors, labeled with a membrane dye. The segmented membrane extensions originating from the centered cell are overlaid in the bottom row. Associated with Fig. 4E.

Movie 10: **WAVE complex-enriched domain dynamics in a *fat2* mosaic epithelium.** A *fat2* mosaic epithelium in which all cells express Sra1-GFP, used to evaluate WAVE complex-enriched domain dynamics in control or *fat2* cells within a migratory context. Associated with Fig. S7B,C.

Movie 11: **Colocalization of puncta of Fat2 and the WAVE complex along leading-trailing interfaces.** The leading-trailing interfaces of two cells expressing Fat2-3xGFP and Abi-mCherry, used to compare the distributions of Fat2 and the WAVE complex over time. The Fat2-3xGFP channel is offset 2 pixels downward so puncta positions can be more easily compared. Associated with Fig. 5B.

Movie 12: **WAVE complex accumulation at side-facing protrusions away from Fat2.** A side-facing cell-cell interface from an epithelium expressing Abi-mCherry and Fat2-3xGFP. Arrows indicate a site of transient Abi-mCherry accumulation, protrusion, and dissipation with no corresponding Fat2-3xGFP enrichment, in contrast to the colocalized Fat2-3xGFP and Abi-mCherry on the leading-trailing interfaces above and below. Associated with Fig. S9.

Supp. Table 1: Key resources

Reagent type (species) or resource	Designation	Source or reference	Identifiers	Additional information
gene (<i>Drosophila melanogaster</i>)	Abi	NA	FLYB:FBgn0020510	FlyBase Name: Abelson interacting protein
gene (<i>Drosophila melanogaster</i>)	Dlg	NA	FLYB:FBgn0001624	FlyBase Name: discs large 1
gene (<i>Drosophila melanogaster</i>)	E-cadherin	NA	FLYB:FBgn0003391	FlyBase Name: shotgun
gene (<i>Drosophila melanogaster</i>)	Ena	NA	FLYB:FBgn0000578	FlyBase Name: enabled
gene (<i>Drosophila melanogaster</i>)	Fat2 (Kug)	NA	FLYB:FBgn0261574	FlyBase Name: kugelei
gene (<i>Drosophila melanogaster</i>)	Lar	NA	FLYB:FBgn0000464	FlyBase Name: Leukocyte-antigen-related-like
gene (<i>Drosophila melanogaster</i>)	Scar	NA	FLYB:FBgn0041781	FlyBase Name: SCAR
gene (<i>Drosophila melanogaster</i>)	Sra1 (CYFIP)	NA	FLYB:FBgn0038320	FlyBase Name: Cytoplasmic FMR1 interacting protein
genetic reagent (<i>Drosophila melanogaster</i>)	Abi-mCherry or ubi>Abi-mCherry	Bloomington Drosophila Stock Center; FLYB:FBrf0227194 (S. Huelsmann)	FLYB:FBst0058729; BDSC:58729	FlyBase Symbol: P{Ubi-mCherry.Abi}3
genetic reagent (<i>Drosophila melanogaster</i>)	abi-RNAi	National Institute of Genetics, Japan	FLYB:FBtp0079430; NIG:9749R	
genetic reagent (<i>Drosophila melanogaster</i>)	E-cadherin-GFP	Bloomington Drosophila Stock Center; PMID:19429710	FLYB:FBst0060584; BDSC:60584	FlyBase Genotype: y[1] w*; T{[T]shg[GFP]}
genetic reagent (<i>Drosophila melanogaster</i>)	GFP-Ena or ubi>GFP-Ena	Bloomington Drosophila Stock Center; FLYB:FBrf0208868 (S. Nowotarski & M. Peiger)	FLYB:FBst0028798; BDSC:28798	FlyBase Genotype: w*; P{Ubi-GFP.ena}3
genetic reagent (<i>Drosophila melanogaster</i>)	ena-RNAi	Vienna Drosophila Resource Center	FLYB:FBst0464896; VDRC:43058	
genetic reagent (<i>Drosophila melanogaster</i>)	Fat2-3xGFP FRT80B	Laboratory of S. Horne-Badovinac; PMID:28292425	FLYB:FBal0326664	FlyBase Symbol: kug[3xGFP]
genetic reagent (<i>Drosophila melanogaster</i>)	Fat2[ΔICD]-3xGFP FRT80B	Laboratory of S. Horne-Badovinac; PMID:28292425	FLYB:FBal0326665	FlyBase Symbol: kug[ΔICD.3xGFP]
genetic reagent (<i>Drosophila melanogaster</i>)	fat2 or fat2[N103-2] FRT80B	Laboratory of Sally Horne-Badovinac; PMID:22413091	FLYB:FBal0267777	FlyBase Symbol: kug[N103-2]
genetic reagent (<i>Drosophila melanogaster</i>)	UAS>Flp	Bloomington Drosophila Stock Center; PMID:9584125	FLYB:FBst0004539; BDSC:4539	FlyBase Genotype: y[1] w*; P{UAS-FLP.D}JD1
genetic reagent (<i>Drosophila melanogaster</i>)	FRT80B	Bloomington Drosophila Stock Center; PMID:8404527	FLYB:FBti0002073	FlyBase Symbol: P{neoFRT}80B
genetic reagent (<i>Drosophila melanogaster</i>)	UAS>F-Tractin-tdTomato	Bloomington Drosophila Stock Center; FLYB:FBrf0226873 (T. Tootle); PMID:24995797	FLYB:FBst0058989; BDSC:58989	FlyBase Genotype: w*; P{UASp-F-Tractin.tdTomato}15A/SM6b; MKRS/TM2
genetic reagent (<i>Drosophila melanogaster</i>)	ubi>GFP-NLS (3L) FRT80B	Bloomington Drosophila Stock Center; FLYB:FBrf0108530 (D. Bilder & N. Perrimon)	FLYB:FBst0001620; BDSC:1620	FlyBase Genotype: w*; P{Ubi-GFP.D}61EF P{neoFRT}80B
genetic reagent (<i>Drosophila melanogaster</i>)	lar[13.2] FRT40A	Bloomington Drosophila Stock Center; PMID:8598047	FLYB:FBst0008774; BDSC:8774	
genetic reagent (<i>Drosophila melanogaster</i>)	lar[bola1]	Bloomington Drosophila Stock Center; PMID:11688569	FLYB:FBst0091654; BDSC:91654	
genetic reagent (<i>Drosophila melanogaster</i>)	MKRS hsFLP/TM6b, Cre	Bloomington Drosophila Stock Center	FLYB:FBst0001501; BDSC:1501	y[1] w[67c23]; MKRS, P{hsFLP}86E/TM6B, P{Crew}DH2, Tb[1]
genetic reagent (<i>Drosophila melanogaster</i>)	nanos-Cas9	Bloomington Drosophila Stock Center; FLYB:FBrf0223952 (F. Port & S. Bullock); PMID:25002478	FLYB:FBst0054591; BDSC:54591	FlyBase Genotype: y[1] M{nos-Cas9.P}ZH-2A w*
genetic reagent (<i>Drosophila melanogaster</i>)	ubi>mRFP-NLS (3L) FRT80B	Bloomington Drosophila Stock Center; FLYB:FBrf0210705 (J. Lipsick)	FLYB:FBti0129786; BDSC:30852	FlyBase Genotype: w1118; P{Ubi-mRFP.nls}3L P{neoFRT}80B

Supp. Table 1: Key resources

716				
genetic reagent (Drosophila melanogaster)	FRT82b ubi>mRFP-NLS (3R)	Bloomington Drosophila Stock Center; FLYB:FBfr0210705 (J. Lipsick)	FLYB:FBst0030555; BDSC:30555	FlyBase Genotype: w1118; P{neoFRT}82B P{Ubi-mRFP.nls}3R
genetic reagent (Drosophila melanogaster)	Sra1-GFP	this paper		
genetic reagent (Drosophila melanogaster)	Sra1-GFP FRT80B	this paper		
genetic reagent (Drosophila melanogaster)	sra1-RNAi	Bloomington Drosophila Stock Center; PMID:21460824	FLYB:FBst0038294; BDSC:38294	FlyBase Genotype: y[1] sc ^v [1] sev[21]; P{TRiP.HMS01754} attP2
genetic reagent (Drosophila melanogaster)	TJ>Gal4	National Institute of Genetics, Japan; PMID:12324948	FLYB:FBtp0089190; DGRC:104055	FlyBase Symbol: P{tj-GAL4.U}
genetic reagent (Drosophila melanogaster)	w1118	Bloomington Drosophila Stock Center	FLYB:FBal0018186	
antibody	Discs Large; Dlg	Developmental Studies Hybridoma Bank	DSHB:4F3; RRID:AB_528203	
antibody	Scar	Developmental Studies Hybridoma Bank	AB_2618386	1:200
antibody	Alexa Fluor™ 647, donkey anti-mouse secondary	Thermo Fisher Scientific	Cat:A31571; RRID:AB_162542	1:300, 3 hrs at room temp
chemical compound, drug	CellMask™ Orange Plasma Membrane Stain	Thermo Fisher Scientific	Cat:C10045	1:250, 15 min
chemical compound, drug	CellMask™ Deep Red Plasma Membrane Stain	Thermo Fisher Scientific	Cat:C10046	1:250, 15 min
chemical compound, drug	TRITC Phalloidin	Millipore Sigma	Cat:1951	1:300, 15 min at room temp
chemical compound, drug	Alexa Fluor™ 647 phalloidin	Thermo Fisher Scientific	Cat:A22287	1:50, 3 hrs at room temp
chemical compound, drug	CK-666, Arp2/3 complex inhibitor	Millipore Sigma	Cat:553502	750 µM
chemical compound, drug	Formaldehyde, 16%, methanol free, ultra pure	Polysciences	Cat:18814-10	
chemical compound, drug	Recombinant human insulin	Millipore Sigma	Cat:12643	
recombinant DNA reagent	plasmid: pU6-BbsI-chiRNA	Addgene	Addgene:45946; RRID:Addgene_45946	PMID:23709638
recombinant DNA reagent	plasmid: pU6 chiRNA Sra1 C-term	this paper		CRISPR chiRNA construct for generation of Sra1-GFP
recombinant DNA reagent	plasmid: pDsRed-attP	Addgene	Addgene:51019	Vector used to make pDsRed-attP Sra1-GFP HR
recombinant DNA reagent	plasmid: pTWG	Drosophila Genome Resource Center	DGRC:1076	source of enhanced GFP for generation of Sra1-GFP
recombinant DNA reagent	plasmid: pDsRed-attP Sra1-GFP HR	this paper		CRISPR homologous recombinaton construct for generation of Sra1-GFP
software, algorithm	Zen Blue	Zeiss		
software, algorithm	MetaMorph	Molecular Devices		
software, algorithm	FIJI (ImageJ)	PMID:22743772		
software, algorithm	GraphPad Prism 9 for Mac	GraphPad Software		
software, algorithm	Microsoft Excel for Mac, version 16.47	Microsoft		
software, algorithm	Python 3	Python Software Foundation		https://www.python.org
software, algorithm	imageio	imageio contributors		https://imageio.readthedocs.io/
software, algorithm	matplotlib	The Matplotlib Development team		https://matplotlib.org/
software, algorithm	napari	napari contributors		https://napari.org/
software, algorithm	numpy	numpy contributors		https://numpy.org/
software, algorithm	pims	pims contributors		http://soft-matter.github.io/pims/v0.5/
software, algorithm	pandas	pandas contributors		https://pandas.pydata.org/
software, algorithm	scikit-image	scikit-image development team		https://scikit-image.org/

Supp. Table 1: Key resources

⁷¹⁷ software, algorithm	scikit-fmm	scikit-fmm contributors	https://pythonhosted.org/scikit-fmm/
software, algorithm	scipy	scipy contributors	https://scipy.org/

Supp. Table 2: Genotypes of experimental females

Figure	Panel	Name	Genotype
2 718	A-C	Control	w1118
		<i>fat2</i>	w;; <i>fat2</i> ^{N103-2} FRT80B
		CK-666	w1118
	D	Control	w1118
<i>fat2</i>		w;; <i>fat2</i> ^{N103-2} FRT80B	
3	B	Sra1-GFP mosaic	w; tj>Gal4 ^{DGRC:104055} , UAS>Flp ^{BDSC:4539/+} ; FRT82B Sra1-GFP/FRT82B ubi>mRFP-NLS ^{BDSC:30555}
	C	<i>fat2</i> mosaic	w; tj>Gal4 ^{DGRC:104055} , UAS>Flp ^{BDSC:4539/+} ; <i>fat2</i> ^{N103-2} FRT80B/ubi>GFP-NLS FRT80B ^{BDSC:1620}
	D-F	<i>fat2</i> mosaic + Sra1	w; tj>Gal4 ^{DGRC:104055} , UAS>Flp ^{BDSC:4539/+} ; <i>fat2</i> ^{N103-2} FRT80B Sra1-GFP/ubi>mRFP-NLS FRT80B ^{BDSC:30852}
4	A	Sra1-GFP mosaic + <i>fat2</i>	w; tj>Gal4 ^{DGRC:104055} , UAS>Flp ^{BDSC:4539/+} ; <i>fat2</i> ^{N103-2} FRT80B FRT82B Sra1-GFP/ <i>fat2</i> ^{N103-2} FRT80B FRT82B
	B,D	Control	w;; Sra1-GFP/+
		<i>fat2</i>	w;; <i>fat2</i> ^{N103-2} FRT80B Sra1-GFP/ <i>fat2</i> ^{N103-2} FRT80B
	E	Control	w1118
		<i>fat2</i>	w; <i>fat2</i> ^{N103-2} FRT80B
5	A,E	Fat2 + Abi	w;; ubi>Abi-mCherry ^{BDSC:58729} , Fat2-3xGFP FRT80B/ Fat2-3xGFP FRT80B
		Fat2 ^{ΔICD} + Abi	w;; ubi>Abi-mCherry ^{BDSC:58729} , Fat2 ^{ΔICD} -3xGFP FRT80B/Fat2-3xGFP FRT80B
	B	Fat2 + Abi	w;; ubi>Abi-mCherry ^{BDSC:58729} , Fat2-3xGFP FRT80B/ Fat2-3xGFP FRT80B
	C,D,F,G	Fat2 + Abi + F-actin	w;; ubi>Abi-mCherry ^{BDSC:58729} , Fat2-3xGFP FRT80B/ Fat2-3xGFP FRT80B
S1	Top row	Protrusion in 1 direction	w1118
	Bottom row	Protrusion in both directions	w; <i>fat2</i> ^{N103-2} FRT80B
S2	A	Control	w1118
		<i>fat2</i>	w;; <i>fat2</i> ^{N103-2} FRT80B
		CK-666	w1118 (treated with 750 μM CK-666)
	B	Control	w1118
<i>fat2</i>		w;; <i>fat2</i> ^{N103-2} FRT80B	
S3	A-C	Control	w; tj>Gal4 ^{DGRC:104055/+}
		<i>fat2</i>	w; tj>Gal4 ^{DGRC:104055/+} ; <i>fat2</i> ^{N103-2} FRT80B
		<i>abi</i> -RNAi	w; tj>Gal4 ^{DGRC:104055/+} ; UAS> <i>abi</i> -RNAi ^{NIG:9749R-3/+}
	D	Control	w; tj>Gal4 ^{DGRC:104055/UAS>F-Tractin-tdTomato} ^{BDSC:58989}
		<i>fat2</i>	w; tj>Gal4 ^{DGRC:104055/UAS>F-Tractin-tdTomato} ^{BDSC:58989} ; <i>fat2</i> ^{N103-2} FRT80B
		<i>abi</i> -RNAi	w; tj>Gal4 ^{DGRC:104055/UAS>F-Tractin-tdTomato} ^{BDSC:58989} ; UAS> <i>abi</i> -RNAi ^{NIG:9749R-3/+}
E,F	Control	w1118	
	<i>fat2</i>	w;; <i>fat2</i> ^{N103-2} FRT80B	
S4	A,B	<i>fat2</i> mosaic	w; tj>Gal4 ^{DGRC:104055} , UAS>Flp ^{BDSC:4539/+} ; <i>fat2</i> ^{N103-2} FRT80B/ubi>GFP-NLS FRT80B ^{BDSC:1620}
S5	A	Sra1-GFP	w;; Sra1-GFP
		anti-SCAR	w1118
		ubi>Abi-mCherry	w;; ubi>Abi-mCherry ^{BDSC:58729/+}
	B	Control	w; tj>Gal4 ^{DGRC:104055/+}
		<i>abi</i> -RNAi	w; tj>Gal4 ^{DGRC:104055/+} ; UAS> <i>abi</i> -RNAi ^{NIG:9749R-3/+}
	C	Control	w1118
Sra1-GFP x1		w;; Sra1-GFP/+	

Supp. Table 2: Genotypes of experimental females

719		Sra1-GFP x2	w;; Sra1-GFP
		<i>sra1</i> -RNAi	w; tj>Gal4 ^{DGRC:104055/+} ; UAS> <i>sra1</i> -RNAi ^{BDSC:38294/+}
	D	Control	w1118
		Sra1-GFP x1	w;; Sra1-GFP/+
		Sra1-GFP x2	w;; Sra1-GFP
S6	A,C-E	Control	w;; Sra1-GFP/+
		<i>fat2</i>	w;; <i>fat2</i> ^{N103-2} FRT80B Sra1-GFP/ <i>fat2</i> ^{N103-2} FRT80B
S7	A	Control	w;; Sra1-GFP/+
		<i>fat2</i>	w;; <i>fat2</i> ^{N103-2} FRT80B Sra1-GFP/ <i>fat2</i> ^{N103-2} FRT80B
	B,C	<i>fat2</i> mosaic + Sra1	w; tj>Gal4 ^{DGRC:104055} , UAS>Flp ^{BDSC:4539/+} ; <i>fat2</i> ^{N103-2} FRT80B Sra1-GFP/ubi>mRFP-NLS FRT80B ^{BDSC:30852}
S8	A,B	Control Fat2 + Abi	w;; ubi>Abi-mCherry ^{BDSC:58729} , Fat2-3xGFP FRT80B/ Fat2-3xGFP FRT80B
		<i>ena</i> -RNAi, Fat2 + Abi	w; tj>Gal4 ^{DGRC:104055} /UAS> <i>ena</i> -RNAi ^{VDRC:43058} ; ubi>Abi-mCherry ^{BDSC:58729} , Fat2-3xGFP FRT80B/ Fat2-3xGFP FRT80B
		<i>lar</i> Fat2 + Abi	w; <i>lar</i> ^{bola1} BDSC:91654/ <i>lar</i> ^{13.2} BDSC8774 FRT40A; ubi>Abi-mCherry ^{BDSC:58729} , Fat2-3xGFP FRT80B/ Fat2-3xGFP FRT80B
		Control E-cadherin + Abi	w; Shg-GFP ^{BDSC:60584/+} ; ubi>Abi-mCherry ^{BDSC:58729/+}
	C-E	Ena + Abi + F-actin	w; ubi>GFP-Ena ^{BDSC:28798} /ubi>Abi-mCherry ^{BDSC:58729}
	F	Control	w; tj>Gal4 ^{DGRC:104055/+}
		<i>ena</i> -RNAi	w; tj>Gal4 ^{DGRC:104055} /UAS- <i>ena</i> -RNAi ^{VDRC:43058}
		<i>abi</i> -RNAi	w; tj>Gal4 ^{DGRC:104055/+} ; UAS- <i>abi</i> -RNAi ^{NIG:9749R-3/+}
	G	Control	w;; ubi>Abi-mCherry ^{BDSC:58729} , Fat2-3xGFP FRT80B/ Fat2-3xGFP FRT80B
		<i>lar</i>	w; <i>lar</i> ^{bola1} BDSC:91654/ <i>lar</i> ^{13.2} BDSC8774 FRT40A; ubi>Abi-mCherry ^{BDSC:58729} , Fat2-3xGFP FRT80B/ Fat2-3xGFP FRT80B
	S9		Fat2 + Abi

Supp. Table 3: *Drosophila* culture conditions for experiments

720

Figure	Panel	Days on yeast	Temp (°C)
2	A-D	2-3	25
3	B	7	25
	C	3	25
	D-F	3	25
4	A	5	25
	B,D	2-3	25
	E	2-3	25
5	A,E	2-3	25
	B	2-3	25
	C,D,F,G	2-3	25
S1	A-F	2-3	25
S2	A,B	2-3	25
S3	A-C,E,F	2-3	29
	D	2-3	29
S4	A,B	3	25
S5	A	2-3	25
	B	3	29
	C	3	29
	D-F	2-3	25
S6	A-E	2-3	25
S7	A	2-3	25
	B,C	3	25
S8	A,B,G	3	29
	C-E	2-3	25
	F	3	29
S9		2-3	25